Experimental Investigation of Particle Flow in a Spiral Concentrator

Zhou Tong Deng

Department of Mining and Materials Engineering
McGill University
Montreal, Canada

January 2015

A thesis submitted to McGill University
in partial fulfillment of the requirement of the degree of
Master of Engineering

Abstract

The spiral concentrator is a mineral processing device that separates mineral particles according to their densities and to a lesser extent particle size. In this thesis, a four-turn WALKABOUT PW1 spiral concentrator was used to investigate the particle movement inside the trough of spiral concentrator. For the experiments, a synthetic ore was prepared to mimic a real iron ore from Mont-Wright (Quebec). The sample consisted of 40% magnetite ($\rho = 5.17$ g/cm^3) and 60% quartz ($\rho = 2.65$ g/cm^3) with a size range smaller than 850 µm. In order to produce a comprehensive data set of particle distribution across the trough in every turn of spiral concentrator, the material was sampled at the end of every turn.

The separation of mineral particles observed was as described in the literature, with small and dense particles tending towards the centre of the spiral, on the other hand, large light particles tending towards the outside of the spiral; and a small portion of the large heavy particles would report to the outside. The flow rate and physical properties of the slurry were analyzed from the sampled materials. A database produced from the experiment was used to build partition curves of the magnetite and quartz for every turn of the spiral. A partition curve model was applied to predict the recovery of magnetite in the virtual fifth turn of the spiral. The understanding of the separation mechanism gained in this study will be of interest to improve the design of spiral concentrator and to adjust the operational parameters of mineral concentration.

Résumé

Le spiral concentrateur est un dispositif de traitement du minerai qui peut séparer des particules minérales en fonction de leur densité et de la taille des particules. Dans cette thèse, un quatre tours WALKABOUT PW1 spirale concentrateur a été utilisée pour étudier le mouvement des particules à l'intérieur de la gouttière de concentrateur spirale. Pour réaliser les expériences, un échantillon artificielle a été préparé à imiter un véritable échantillon de minerai de fer de Mont-Wright, l'échantillon artificielle se compose de 40% de magnétite (ρ = 5,17) et 60% de quartz (ρ = 2,65) dans la gamme de taille plus petit que 850 μm. Afin de produire un ensemble de données complet de la distribution des particules à travers la gouttière de chaque tour de concentrateur spirale, le matériel a été échantillonné à la fin de chaque tour de la gouttière.

La séparation des particules minérales observée était telle que décrite dans la littérature, où les particules petites et lourdes tendant vers le centre de la spirale, d'autre part, les particules grosses et légeres tendant vers l'extérieur de la spirale; et une petite partie des grosses particules lourdes ont été exceptionnellement être transportés à l'extérieur. Le débit et les propriétés physiques de la suspension ont été analysés à partir des matériaux de l'échantillon. Une base de données produite à partir des expériences a été utilisé pour construire les courbes de séparation de la magnétite et de quartz pour chaque tour de la spirale. Un modèle de courbe de séparation était appliquée à prédire la récupération de la magnétite dans le cinquième tour de la spirale virtuel. La compréhension du mécanisme de séparation acquise dans cette étude sera d'intérêt pour améliorer la conception de concentrateur spirale et d'ajuster les paramètres de fonctionnement de la concentration du minérai.

Acknowledgements

I would like to take this opportunity to thank all the people that have helped this project come to life;

First of all, to my supervisor, Professor Kristian E. Waters, thank you for giving me this opportunity to pursue my master's degree, providing constant encouragement and patient guidance to my work.

Many thanks to Mr. Darryel Boucher for the continuous support on setting up the apparatus and conducting the experiments.

Special thanks to Mr. Ray Langlois, for providing various technical support and a joyful working environment.

I would thank COREM and the Natural Sciences and Engineering Research Council of Canada for the financial support.

I would like to acknowledge all colleagues in the McGill Mineral Processing Group for help and a good time.

Finally, I would like to thank all of my family and friends for the support and encouragement.

Table of Contents

Abstract i

Résumé ii

Acknowledgement iii

Table of Contents iv

List of Figures vi

List of Tables ix

Chapter 1 - Introduction and Problem Statement 1

Chapter 2 - Theory and Literature 3

2.1 Introduction of Spiral Concentrator 3

- 2.1.1 History of Spiral Concentrator 3
- 2.1.2 Feature and Operation of Spiral Concentrator 4

2.2 Mechanism of Separation 8

- 2.2.1 Concentration Criterion 8
- 2.2.2 Physical Properties of Slurries 9
- 2.2.3 Settling 11
- 2.2.4 Bagnold Force 13
- 2.2.5 Secondary Flow 19

2.3 Profiles of Primary Flow of Spiral Concentrator 22

- 2.3.1 Laminar Flow 23
- 2.3.2 Smooth Turbulent Flow 25
- 2.3.3 Rough Turbulent Flow 25
- 2.3.4 The Suspension Flow 26
- 2.3.5 The Manning Profile 26
- 2.3.6 The Flow Incorporating Particle Effect 28

2.4 Data Interpretation 30

- 2.4.1 Mineral Recovery vs. Total Mass Recovery Plots 30
- 2.4.2 Efficiency Plots 31
- 2.4.3 The Upgrade Ratio vs. Total Mass Recovery Plots 32
- 2.4.4 Partition Curves 33

2.4.5 Comparison of Data Treatments 35
2.5 Performance Models of Spiral Concentrators 36
2.5.1 The Holland-Batt Model 36
2.5.2 The Das Model 38
2.5.3 The Tucker Model 40
2.5.4 The Bazin Model 41
Chapter 3- Experimental Procedure 43
3.1 Sample Preparation 43
3.2 The Closed Loop Experimental Set-Up 44
3.3 Slurry Splitting and Collection 46
3.4 Slurry Analysis 49
3.5 The Profile Gauge 49
3.6 Profile Measurement 50
Chapter 4 - Results and Discussion 51
4.1 Flow Rate 51
4.2 Flow Height 54
4.3 Flow Speed 55
4.4 Physical Properties of the Slurry 56
4.5 Performance and Efficiency 58
4.6 Mineral Recovery vs. Concentrate Grade Plots 59
4.7 Partition Curves of Magnetite and Quartz 62
4.8 Modeling of Partition Curves of Magnetite 68
Chapter 5 - Conclusion and Recommendation 75
Reference 78
Appendix 82

List of Figures

Figure 1 - Pictorial view of spiral concentrator 3

Figure 2 - Recovery of minerals as a function of particle size for spiral concentrator .. 6

Figure 3 - The splitters of a spiral concentrator (Mine-Engineer.Com, 1994-2012) 7

Figure 4 - The Concentration Criterion of various ores at different particle size (Burt, 1984) 9

Figure 5 - Particle-particle interactions in fluid transport (Bagnold, 1954) 17

Figure 6 - Secondary flow behavior of spiral concentrator(Holland-Batt, 1987) 20

Figure 7 - Secondary flow visualization by dye injection (Holtham, 1990) 21

Figure 8 - The velocity profile of the flow on a spiral concentrator summarized by (Holland-Batt, 1987) 27

Figure 9 - Example of a mineral recovery vs. total mass recovery 31

Figure 10 - Example of an efficiency plot 32

Figure 11 - Example of an Upgrade ratio vs. total mass recovery plot 33

Figure 12 - Measured partition factors as a function of particle size for various splitter positions (King et al., 1992) 34

Figure 13 - Partition curves for the spirals of the Lac Bloom concentrator on two different stages (Bazin et al., 2014) 35

Figure 14 - Durand relationship for Fd (Holland-Batt, 1992a) 38

Figure 15 - Effect of relative specific gravity on the radial distribution of particle size (Das et al., 2007) 39

Figure 16 - Structure of the empirical model for a spiral concentrator (Bazin et al., 2014) 41

Figure 17 - Size distribution of the iron ore sample from Mont-Wright. 43

Figure 18 - The grade of hematite of all particle size fractions of the iron ore sample from Mont-Wright 44

Figure 19 - The WALKABOUT PW1 spiral concentrator 45

Figure 20 - Schematic sketch of the experimental set-up 46

Figure 21 - a) slurry sampling locations in spiral b) cross-sectional view of the trough of spiral 47

Figure 22 - a) Top view of Collector A b) Side view of Collector A 48

Figure 23 - Collector B for sampling the slurry from T channel 49

Figure 24 - The profile gauge 50

Figure 25 - The mass flow of solids..51

Figure 26 - The flow rate of each channel in each turn of the spiral 53

Figure 27 - The profiles of the trough..54

Figure 28 - The flow heights...55

Figure 29 - Mineral recovery vs. total mass recovery 58

Figure 30 - The efficiency of the separation..59

Figure 31 - The recovery of magnetite 60

Figure 32 - The grade of magnetite of each channel in each turn of the spiral 61

Figure 33 - Cumulative grade of magnetite vs. cumulative recovery of magnetite.....62

Figure 34 - Partition curves for magnetite of C1 channel..64

Figure 35 - Partition curves for magnetite of C2 channel..64

Figure 36 - Partition curves for magnetite of C3 channel..65

Figure 37 - Partition curves for magnetite of T channel..65

Figure 38 - Partition curves for quartz of C1 channel 66

Figure 39 - Partition curves for quartz of C2 channel 67

Figure 40 - Partition curves for quartz of C3 channel 67

Figure 41 - Partition curves for quartz of T channel..68

Figure 42 - Observed (symbols) and modeled (lines) partition curves for magnetite on each turn of the spiral concentrator..70

Figure 43 - S_C as a function of the particle size...71

Figure 44 - P_R as a function of the particle size...71

Figure 45 - The recommended operating parameter and the actual operating point ...72

Figure 46 - Alpha S and Alpha P as function of number of turns 73

Figure 47 - d50 s and d50 p as function of number of turns..74

Figure 48 - The modeled partition curves...74

List of Tables

Table 1 - Shear rate for the different Bagnold regimes on LD9 coal spiral................18

Table 2 - Shear rate for the different Bagnold regimes on FGL heavy mineral spiral 18

Table 3 - Grade of chromite (percentage by mass) (Loveday, 1993) 22

Table 4 - The shear rate and N_B calculated by (Loveday, 1993) 30

Table 5 - The mass flow rate of solid and water (g/s) 51

Table 6 - The volumetric flow rate of the slurry (cm^3/s)...53

Table 7 - The mean flow height in different channels and turns (mm) 55

Table 8 - The mean cross-sectional area of the flow (cm^2) 56

Table 9 - The velocity of the flow (cm/s) 56

Table 10 - The weight fraction of the magnetite, quartz and water in the slurry.........56

Table 11 - The density of solid in each channel (g/cm^3) 57

Table 12 - The density of the slurry in each channel (g/cm^3).....................................57

Table 13 - The viscosity of the slurry in each channel (mPa s)..................................57

Table 14 - Parameters for the partition curve models..70

Table 15 - Magnetite recovered in Turn 1 for each channel (g) 82

Table 16 - Magnetite recovered in Turn 2 for each channel (g) 82

Table 17 - Magnetite recovered in Turn 3 for each channel (g) 82

Table 18 - Magnetite recovered in Turn 4 for each channel (g) 83

Table 19 - Quartz recovered in Turn 1 for each channel (g) 83

Table 20 - Quartz recovered in Turn 2 for each channel (g) 83

Table 21- Quartz recovered in Turn 3 for each channel (g) 84

Table 22 - Quartz recovered in Turn 4 for each channel (g) 84

Chapter 1 - Introduction and Problem Statement

The spiral concentrator is one of the most common gravity concentration devices used in the mineral processing industry to recover valuable heavy minerals from gangue. Over the past few decades, spiral concentrators have been used effectively to treat coal and beach sand. Today, it is successfully used to beneficiate a number of ores including chromite, rutile, gold ore, iron ore, etc., mainly due to its operational simplicity and cost effectiveness. Recently, there has been an accelerated growth in the use of spirals for iron ore beneficiation (Mishra and Tripathy, 2010).

The structure of the spiral is simple; its major component is an open trough, and possesses no moving part. Despite its apparent simplicity, the separation mechanism which occurs in a spiral concentrator is complex. Many researchers have conducted investigations to understand the particle separation mechanism of spirals (Glass et al., 1999; Holland-Batt, 1995; Holland-Batt and Holtham, 1991; Richards et al., 2000; Sivamohan and Forssberg, 1985). However, most investigations only studied the recovery of heavy particles in the concentrate stream from results collected at the output of the spiral; limited literature is available on the studies of particle movement inside the spiral concentrator. Atasoy and Spottiswood (1995) studied particle movement in 3 spirals with different number of turns, the effect of size and density of the particles on the movement are explored. The conclusion of their studies shown that a 1 turn spiral provides sufficient time for the separation of coarse particles, to remove dense minerals from small coal particles at small sizes, a full 5 or 6 turns spiral is essential to be employed. Medium sized particles are distributed along the cross-section of the trough in close ratios.

In this study, the investigation of particle movement in a single spiral was undertaken in order to increase the understanding of spiral concentration. In order to do so, the concentrating effects of the particles with different size and specific gravity could be quantified. The objective of the study was to produce a comprehensive data set of particle distribution across the trough in every turn of spiral concentrator by running one spiral with one feed type with a constant experimental condition. The objective was achieved in the following manner:

As will be described in more detail in Chapter 3, synthetic ore was used consisting of quartz ($\rho = 2.65$ g/cm^3) and magnetite ($\rho = 5.17$ g/cm^3) in the size range smaller than 850 µm. The material was sampled at every turn by means of a specially constructed sampling device. The placement of the various sizes and densities of particles across the spiral trough in every turn will be assessed and a mechanism proposed to explain the separation which is achieved.

The study was structured as follows:

Chapter 2, the relevant Theory and Literature will be discussed. In Section 1, the evolution history, the feature as well as the operation of the spiral concentrator will be introduced. Section 2 will discuss the physical mechanisms that explain particle separation in a spiral. Section 3 will introduce various flow profiles that can describe the primary flow on spiral. Section 4 will cover the diverse means of graphically interpreting the results from spiral test. In the end, a series of modelling describing the concentration performance of spirals will be introduced in Section 5.

Chapter 3, Material and Experimental Procedure, will describe the equipment and sampling device used to perform the experiment. The methodology of the test program will also be described.

Chapter 4, Result and Discussion, will present graphically the results collected from the experiment. The qualitative and quantitative observation will be described.

Chapter 5, Conclusion, will summarise the finding of this study and make a recommendation for the future study based on the findings.

Chapter 2 - Theory and Literature

2.1 Introduction of Spiral Concentrator

2.1.1 History of Spiral Concentrator

A typical spiral concentrator consists of an open trough that twists downward in a helix form about a central column (see Figure 1).

Figure 1 - Pictorial view of spiral concentrator

The Humphreys Spiral was the first spiral concentrator developed by I.B. Humphreys in Denver, Colorado in 1943 and it is remained the only type on the market for many years (Burt, 1984). Humphreys manufactured a range of spirals; the original Humphreys Spiral was made of cast iron, was about 60 cm in diameter, and had five complete turns of the helix, the coal spiral has six complete turns with a slightly flatter pitch. The spiral consists of helical sluice of modified semi-circular cross section wrapped around a central supporting column, in most of spiral, the central column is also considered to be the discharge pipe for collected concentrate.

The early models of spiral usually required wash water; the wash water channel is located inside the main concentrating channel. The wash water is an important control variable used to wash away entrapped light minerals from the concentrate, and this effect is mainly located on coarse particles (Sadeghi et al., 2014). The advantage of wash water spirals is able to produce clean slim-free concentrate, however, the disadvantage is multiple feed points require good distribution (Falconer, 2003); in addition, these wash water distribution systems suffer from a tendency to block. (Richards and Palmer, 1997) indicate significant benefits were observed after the removal of wash water from spirals treating light minerals. Therefore, wash water system is removed from the design of modern spiral concentrator

In the early 1980s, a new generation of spirals made of fiberglass and polyurethane were developed for the Australian beach sand industry (Fuerstenau and Han, 2003). Further, a second spiral wrap just below the turns of the first spiral (called multiple starts) can double the capacity per floor area. In these cases, twin helical spirals are intertwined around the central column, each spiral being 180 degrees out of phase with the other. Wall height is reduced to accommodate the double start arrangement whilst maintaining a constant pitch. The new generation spirals have modified profiles and concentrate cutters that eliminated the need for wash water. The advantage of wash waterless spiral is reducing the consumption of water, which is an important operating consideration especially for the dry areas such as Australia and Africa. The device has been used for both roughing and cleaning.

2.1.2 Feature and Operation of Spiral Concentrator

The typical feed to the spiral concentrator is in a form of pulp, which is a mixture of solid and liquid. The feed is introduced to the spiral via a feed box which is normally placed on top the spiral. The feed box can reduce the velocity of the feed flow and establish a correct pattern of flow. The feed flow entered the spiral is driven by the gravity force. The particles settle down onto the surface of the trough to form a flowing bed across the trough in which the volumetric particle concentration is high. A combination of forces draws heavy particles moving inward to the centre, the heavy particles forms a concentrate band. The lighter particles spread across the remainder of the trough in descending order of specific gravity. The majority of the water flows along the outer edge of the trough (Loveday and Cilliers, 1994). The greater the difference of specific gravity between the valuable mineral and gangue mineral, the better the separation, which will be discussed in detail later in this study.

To operate spiral concentrator , the particle size in the feed is ideally about 75 µm to 1650 µm; however, for coal treatment about 200 µm to 850 µm is preferred (Fuerstenau and Han, 2003). Therefore, the feed preparation is usually employed, which is done with screening. Particle size plays an important role and a feed with a narrow size range will separate more efficiently than one with a broad size range. A number of researchers discovered that the different recovery % for different particle size (Atasoy and Spottiswood, 1995; Bazin et al., 2014; Burt, 1984; Hyma and Meech, 1989; Miller, 1991; Richards et al., 2000), for majority of the heavy minerals, the peak value in recovery occurs in the size range -425+75 µm. Figure 2shows the similar results observed by researchers.

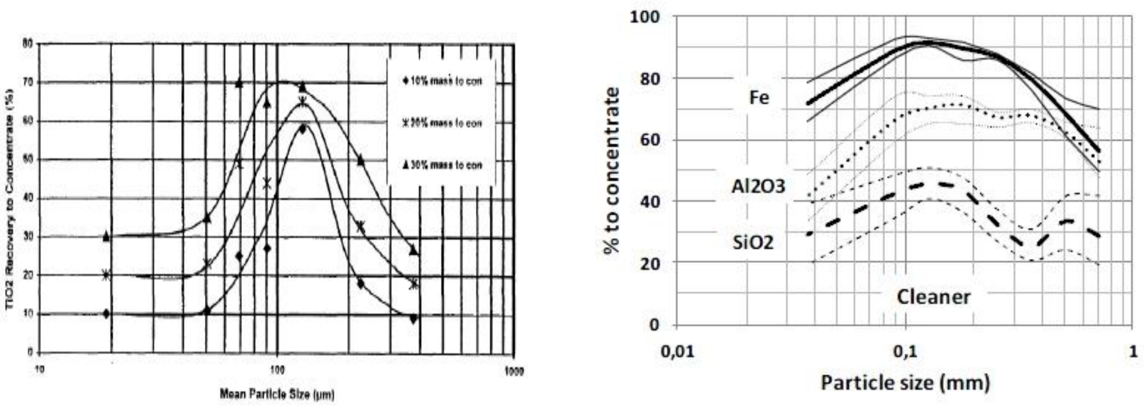

a) (Richards et al., 2000) b) (Bazin et al., 2014)

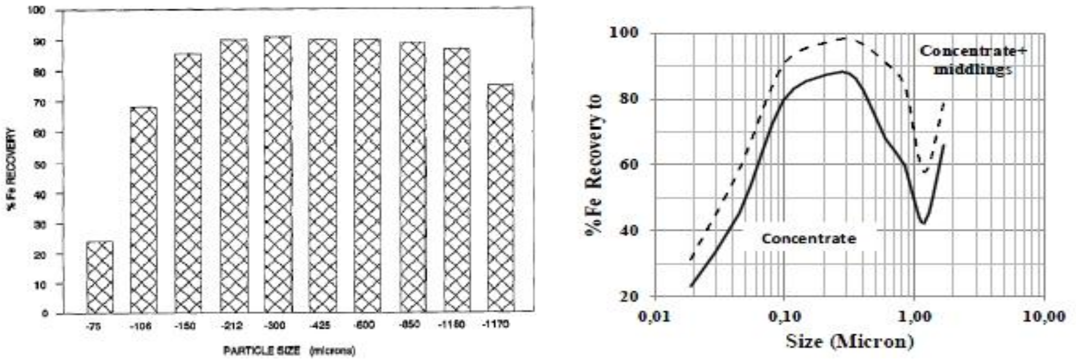

c) (Hyma and Meech, 1989) d) Calculated from (Miller, 1991)

Figure 2 - Recovery of minerals as a function of particle size for spiral concentrator

To discharge the concentrate from spiral concentrators, splitters have to be used. Splitters are located down the length of the trough, which divide a portion of concentrate band from the main flow. Figure 3 shows the splitters of a spiral concentrator which are located in the base. These two splitters divided the main flow into three channels from the inner zone of the trough to the edge respectively, which are concentrate stream, middling stream and tailing stream.

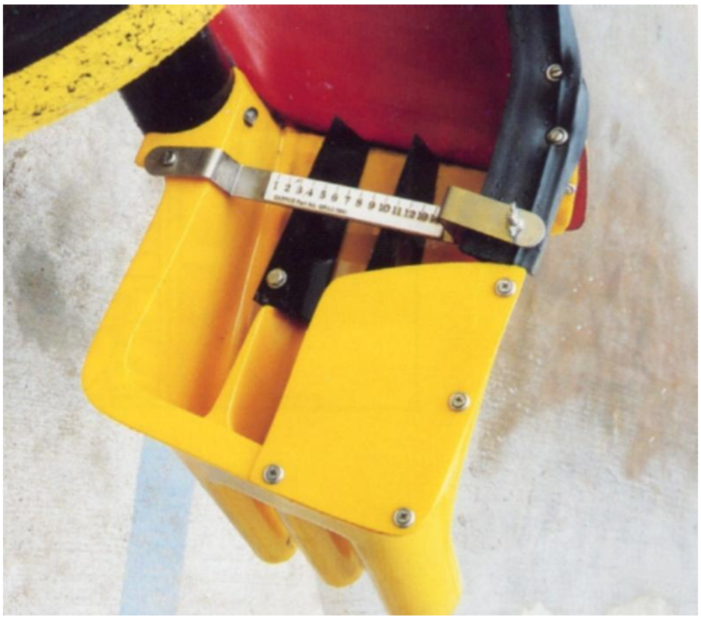

Figure 3 - The splitters of a spiral concentrator (Mine-Engineer.Com, 1994-2012)

By adjusting the position of the splitter, the amount of the pulp stream actually removed to the concentrate can be controlled. The visual inspection of the pulp flow characteristics will generally be a good guide to optimum settings. The removal of concentrate is normally conducted at the base of spiral; however, in certain model of spirals, the discharge of concentrate is performed in every turn of the helix. Since the turbulence from the feed box has been smoothed out in the first half turn of the helix, coarse heavy minerals commence to separate into a discreet band very rapidly; therefore the removal can start by the end of the first turn of the helix (Burt, 1984).

The spiral with a splitter available high up the helix is called a multi-offtake spiral concentrator, and is often used to treat high grade feeds. When treating high grade feeds, over two-third of the concentrate weight can be removed from the top two turns of the helix. Conversely, when treating lower grade feeds, the pulp needs more travelling time for mineral separations to be achieved in the spiral channel, and the extending separation distance can increase the grade of the product removed from port.

The pitch (height loss per revolution), diameter and profile (radial shape) of the trough each play a critical role in the performance of the spiral. When treating feeds with large and heavy particles, the spiral used is generally 60 cm in diameter and 40 cm in pitch. However, when treating fine and lighter particles, the spiral employed is normally of a lower pitch and large diameter, which can provide a lower flow speed and reduces the amount of valuable mineral lost to the tailings.

2.2 Mechanism of Separation

2.2.1 Concentration Criterion

Gravity concentration is one of the oldest mineral processing techniques developed in the human history; it can date back to at least 3000 BC when Egyptians used the technique to separate gold from sand.

To treat an ore with a gravity concentrator, it is necessary to determine the suitability of a gravity concentration process. There are many expressions used to determine the amenability of ores to gravity concentration. One expression which consistently employed is the Concentration Criterion. This is usually defined as:

$$\text{Concentration Criterion (CC)} = \frac{(\rho_h - \rho_f)}{(\rho_l - \rho_f)} \qquad (2.1)$$

Where ρ_h is the specific gravity of the heavy mineral; ρ_h is the specific gravity of the light mineral and ρ_f is the specific gravity of the fluid carrier. The specific gravity is the ratio of the density of a substance to the density of water. To separate two minerals with gravity concentration, the higher the Concentration Criterion is the easier the separation.

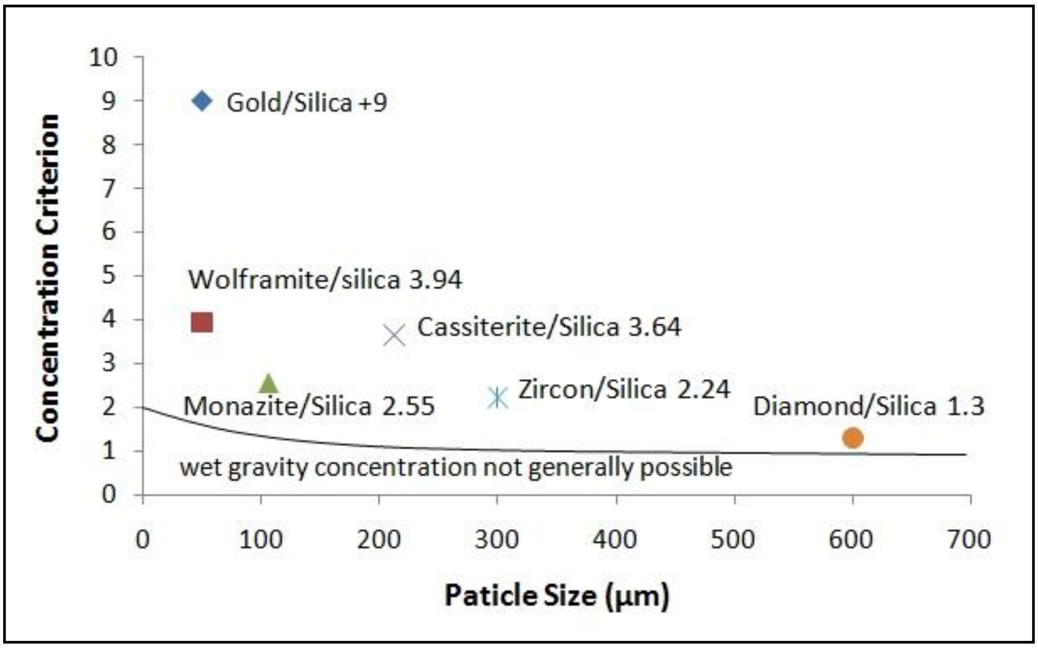

Figure 4 - The Concentration Criterion of various ores at different particle size (Burt, 1984)

The shape of particles cannot be ignored when we use Concentration Criterion. The Concentration Criterion must be multiplied by a shape ratio factor, which is the quotient of the shape settling factor for the heavy mineral and the shape settling factor for the light mineral. The shape settling factor is the ratio of the terminal velocity of two same size particles of the same mineral but with a different shape. The one with the shape that the ratio is required to measure and the other one is spherical. When the particle shape is taken into account the Concentration criterion can be very useful.

2.2.2 Physical Properties of Slurries

Slurry is a fluid mixture of a pulverized solid with liquid. The slurries tend to be Newtonian fluid for low solid concentration, with a limit of 5-7% solid by volume; however, with the solid concentration higher than this value, the fluid becomes Non-Newtonian (Sikdar and Ore, 1979).

The slurries consist of solid particles suspended in a liquid; thus the physical properties of this mixture depend upon the quantity of solid. The density of the slurry can be calculated from the following equation:

$$\rho_m = \frac{100}{\frac{C_w}{\rho_s} + \frac{100 - C_w}{\rho_l}} \qquad (2.2)$$

Where

ρ_m is the density of the slurry (kg/m^3), C_w is the concentration of solids by weight in the slurry (%), ρ_s is the density of solids (kg/m^3), ρ_l is the density of carrier liquid (kg/m^3).

The concentration of the solids by weight (C_w) is usually smaller than the concentration of the solids by volume (C_v) due to the density of solid is higher than the density of liquid. The relationship of these four variables can be expressed as:

$$C_v = C_w \frac{\rho_m}{\rho_s} \qquad (2.3)$$

The viscosity of low solid concentration slurry can be calculated approximately from the volume fraction Φ which can be written as:

$$\mu_m = \mu_l(1 + 2.5\Phi) \qquad (2.4)$$

Where μ_m is the viscosity of the slurry mixture (Pa s), μ_l is the viscosity of the carrier liquid (Pa s). However, Equation 2.4 applies only to laminar flow and solid concentration lower than 1 percent by volume.

For higher solid concentration slurry, the viscosity of the mixture can be calculated by the equation developed by (Thomas, 1965)

$$\mu_m = \mu_l(1 + 2.5\Phi + 10.05\Phi^2 + 0.00273e^{16.6\Phi}) \qquad (2.5)$$

The first three terms of Equation 2.5 account for over 97.5% of the value of the viscosity when $\Phi<25\%$, the fourth term account for the transfer of particles between planes.

2.2.3 Settling

As the pulp flows around in the helical trough of spiral concentrator, stratification occurs in a vertical plane. The stratification is usually considered to the result of hindered settling. The result is that, heavy particles proceed to the lower velocity zones near the trough surface, and the light particles tend to stratify above heavies and move in the higher velocity zones, which is close to the surface of flow.

When a particle is in the status of "free settling", its velocity obeys either Stock's Law (for fine particles) or Newton's Law (for coarse particles). However, as the number of particles increases in the fluid, the effect of particle crowding becomes apparent, the interference between the particles causes a decreasing of the settling rate of the particles. The particles can no longer settling freely, and the system will behave as a heavy liquid with a density of the slurry rather than the fluid, and this is known as "hindered settling" (Burt, 1984).

Newton derived the following equation for the free settling of coarse particles larger than 2 mm:

$$V_t = \left[\frac{4\left(\rho_p - \rho_f\right)dg}{3Q\rho_f}\right]^{1/2} \tag{2.6}$$

In Equation 2.6, V_t represents the terminal velocity of the particle, m/s; Q is the coefficient of resistance, here for a spherical particles $Q = 0.4$; ρ_p is the density of the particle, kg/L; ρ_f is the density of the fluid, kg/L; d is the diameter of the particle, m; g is the acceleration due to the gravity, m/s^2.

Similarly, Stokes derived another relationship for the fine particle (finer than approximately 0.1 mm) free settling in a fluid as follows:

$$V_t = \frac{\left(\rho_p - \rho_f\right)d^2g}{18\mu} \tag{2.7}$$

In Equation 2.7, μ represents the fluid viscosity (mPa s); the rest of symbols are same as in Equation 2.6.

Richardson and Zaki (1954) studied the dynamic equilibrium of a suspension of uniform spherical particles settling in a fluid, and an expression was obtained for the drag force on a constituent particle, this expression is in a form of a correction factor to be used in conjunction with Stokes' Law, which is as follow:

$$V_{hs} = V_t \frac{(\rho_p - \rho_s)}{(\rho_p - \rho_f)} f(\varepsilon) \qquad (2.8)$$

In Equation 2.8, V_{hs} is the velocity of hindered settling for a particle, V_t is the velocity of free settling, ρ_p is the density of the particle, ρ_s is the density of the suspension, ρ_f is the density of the carrier fluid, and $f(\varepsilon)$ is the function represents the effect of particle crowding on the hindered settling velocity. Buoyancy effects on the hindered settling velocity must be considered separately since it is a function of the overall density of the pulp instead of the carrier liquid alone (Richardson and Zaki, 1997).

The velocity of a settling particle can be considered as a function of its specific gravity to water which is $(SG_p - 1)$ and the diameter of the particle. When two particles with the same specific gravity settle in the water, the particle with greater diameter will have the higher terminal velocity. When two particles with the same diameter settle in the water, then the denser particle will have the higher terminal velocity.

Gaudin (1939) showed the ratio of particle size (d_a and d_b) at which two minerals with different density (ρ_a and ρ_b) will have equal terminal settling velocity in free settling condition, this ratio is known as the free settling ratio (R_f)

$$R_f = \frac{d_a}{d_b} = \left[\frac{\rho_b - 1}{\rho_a - 1}\right]^n \qquad (2.9)$$

Where n is a coefficient with a range from 1 for particles settling in the Newtonian regime to 0.5 for particles settling in the Stokesian regime.

As the solid content of the pulp increases, the fluid media becomes a heavy liquid with the density of the slurry rather than the fluid, the term ρ_f the apparent density of the fluid replaces unity in Equation 2.9, and the hindered settling ratio (R_h) is:

$$R_h = \frac{\mathrm{d_a}}{\mathrm{d_b}} = \left[\frac{\rho_b - \rho_f}{\rho_a - \rho_f}\right]^{\mathrm{n}} \qquad (2.10)$$

Hindered settling plays an important role in spiral concentrators, since the concentration of the solids in the feed is high enough for hindered settling to be taking place. Thus, an initial separation of particles leaving the feed box on a spiral will take place as a result of hindered settling (Loveday, 1993).

According to the hindered settling mechanism, in the separation of particles on a spiral, the large dense particles should preferably congregate to the inner zone of the spiral while small light particles move to the outer zone of the spiral. However, in the study of Holtham (1992a), small high density particles tend to migrate to the inside of the spiral trough while large low density particles tend to move to the edge of the trough. This phenomenon revealed that the hindered settling is not the only mechanism that affects the particles separation in spiral concentrator. The next section will introduce another mechanism playing a role in spiral concentrator.

2.2.4 Bagnold Force

When a suspension of particles is subjected to continuous shear, then pressure tends to develop across the plane of shear at right angles to the surface of shear. This phenomenon was originally determined by Bagnold (1954). In spiral concentrators, the fluid in a film flowing under gravity has a velocity profile which increases with the height of the fluid, the particles in the fast flowing upper layer of the fluid will collide with the particles in the slow flowing lower layer of the fluid. The resultant force on a particle from this collision is proportional to the square of particle diameter and also proportional to the rate of shear. Thus the Bagnold force (F_b) can be expressed as:

$$F_b = K_1 r^2 \tag{2.11}$$

Where K_1 is a constant of proportionality, and F_b is Bagnold force which is perpendicular to the plane of flow. When a particle starts to move, the gravitational force will act against the Bagnold force, and the fluid drag force is proportional to the square of particle diameter. At an equilibrium point, a particle moves neither up nor down, where the gravitational force is just equal to the Bagnold force. The gravitational force (F_g) can be written as:

$$F_g = \frac{4}{3}\pi r^3(\rho_p - \rho_f)g \tag{2.12}$$

Where r is the radius of the particle, ρ_p is the density of the particle (g/cm^3), ρ_f is the density of the fluid (g/cm^3), g is the gravitational constant. F_g can be simplified as:

$$F_g = K_2 r^3(\rho_p - \rho_f) \tag{2.13}$$

Where $K_2 = \frac{4}{3}\pi g$,

When the Bagnold force is greater than the gravitational force, F_b - F_g will be positive for upward force resolution, which can be expressed as:

$$F_b - F_g = K_1 r^2 - K_2 r^3(\rho_p - \rho_f) \tag{2.14}$$

This can be rearranged as:

$$F_b - F_g = K_1 r^2[1 - K_3 r(\rho_p - \rho_f)] \tag{2.15}$$

Where $K_3 = K_2/K_1$

It can be seen that the resultant force ($F_b - F_g$) will decrease with increasing particle density and increase with increasing particle size. Therefore, a particle sorting produced by the Bagnold force will be a vertical stratification. Under this stratification, the coarse light particles stay on the top of the flow followed by fine light and coarse heavy particles, the fine heavy particles which experience the least Bagnold dispersive pressure, remain at the bottom of the flow. This type of classification is opposite of hindered settling. However, in spiral concentrator, the shear is produced solely by flow which is depending on the slope of the trough, the rates applied to the particles is limited in a spiral concentrator compare to the other forces (Burt, 1984).

The lifting power of the Bagnold dispersive force is obtained from a factor N, proposed by Bagnold (1954):

$$N = \frac{\lambda^{1/2}\rho_p D^2}{\mu}\frac{du}{dy} \qquad \text{For } \lambda < 14 \tag{2.16}$$

Where ρ_p is the particle density, D is the particle diameter, μ is the viscosity of the carrier fluid, $\frac{du}{dy}$ is the mean shear rate, and λ is the linear concentration as defined in the following equation:

$$\lambda = \frac{1}{(C_o/C)^{1/3} - 1} \tag{2.17}$$

Where C is the volumetric concentration of solids, and C_o is the maximum volumetric concentration that for identical spherical particles packed in a square array, which is equal to $\pi/3\sqrt{2}$ = 0.74

Bagnold (1954) defined two different regimes according to the value of factor N, if N is less than 40, then the regime is dominated by the effects of fluid viscosity, which is called macro-viscous regime; if N is greater than 450, then the regime is dominated by the effects of grain inertia, which is called grain-inertia regime. The regime between these two values is a transition regime, in which the interactions are a combination of collision and viscous motion.

In the “grain-inertial” regime, the Bagnold dispersive pressure P on a particle can be written as:

$$P = 0.042\rho_p(\lambda D)^2\left(\frac{du}{dy}\right)^2\cos\alpha_i \tag{2.18}$$

Where α_i is the angle at which the particles of two adjacent layers collide with each other.

Bagnold (1954) found the angle α_i is approximately constant at 17.7 degree from the vertical for the grain inertia regime in the system developed by him. Therefore, Equation 2.18 can be expressed as follow by substituting the value of α_i:

$$P = 0.04\rho_p(\lambda D)^2\left(\frac{du}{dy}\right)^2 \tag{2.19}$$

In the macro-viscous regime, the Bagnold dispersive pressure was found to be；

$$P = 1.3(1+\lambda)(1+0.5\lambda)\mu\left(\frac{du}{dy}\right) \tag{2.20}$$

In Equation 2.20, the diameter and density of the particle are not involved. Stresses are transmitted by interstitial fluid friction and are therefore dependent only on fluid viscosity but are independent of particle density. Based on experimental observations, Bagnold (1954) proposed the empirical relationship of shear stress:

$$\tau_{xz} = \lambda^{1.5}\mu\left(\frac{du}{dy}\right) \tag{2.21}$$

And the relationship of dispersive stress:

$$\tau_{zz} = 1.3\tau_{xz} \tag{2.22}$$

Where

τ_{zz} and τ_{xz} are shown schematically in Figure 5:

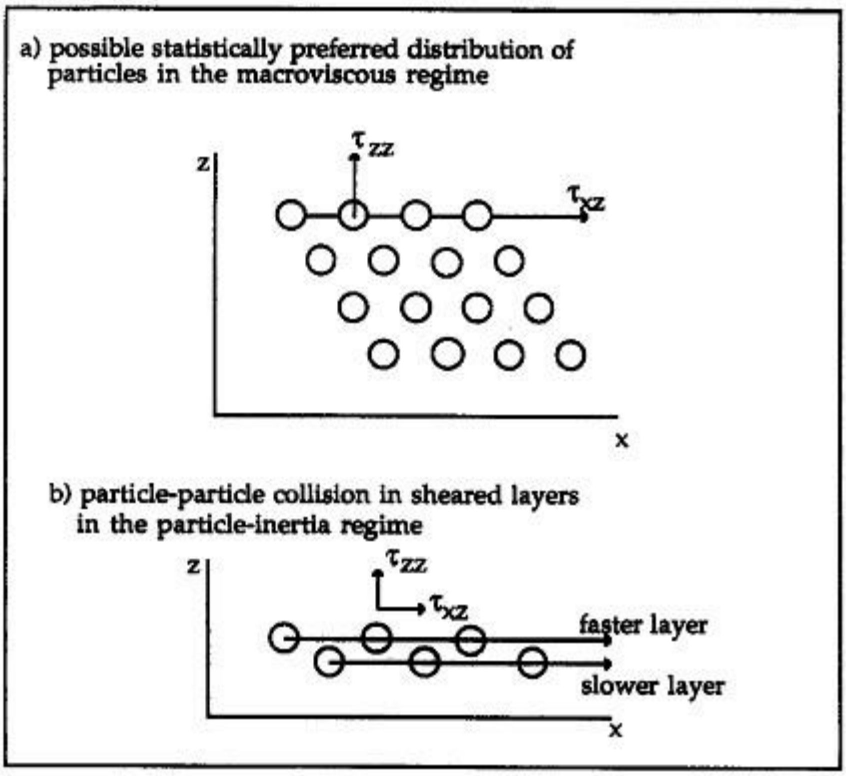

Figure 5 - Particle-particle interactions in fluid transport (Bagnold, 1954)

Figure 5 a) shows that the stresses τ_{zz} are linearly dependent on shear rate τ_{xz} but independent of particle size and density since the absence of collision between particles. Figure 5 b) shows that the dominant effects are particle-particle collisions between the two adjacent layers, in this case, the interstitial fluid plays only a minor role (Bagnold, 1954; Hanes and Inman, 1985).

Holtham (1992a) performed experiments with a feed consisting of silica and water at 15% solids concentration (by mass) on both LD9 coal spiral and FGL heavy mineral spirals. The objective of his study was to verify the applicability of the Bagnold macro-viscous and grain-inertia particle interaction regime. The fluid mean velocity, mean particle size and volumetric concentration were measured at various radial positions across the trough. A multi-stream sampler was placed at the foot of the spiral which can split the main stream into eight sub-streams. The shear rates required to create the two Bagnold interactions (N=40 or N=450) were calculated.

The results generated by Holtham (1992a) are shown in the following tables, the maximum concentration C_{max} is assumed to be 0.558 according to (Allen, 1985), the particle density ρ_p is 2650 kg/m^3, the viscosity of the fluid is 0.00106 Pa s, D is the particle D_{50} value (μm) and C is the measured volumetric concentration in each stream, the λ is calculated using Equation 2.13:

Table 1 - Shear rate for the different Bagnold regimes on LD9 coal spiral

Stream	1	2	3	4	5	6	7	8
D_{50} (μm)	560	560	375	750	880	95	45	28
Vol. Conc.	0.49	0.51	0.56	0.13	0.03	0.02	0.01	0
λ^1/2	4.69	5.34	3.86	1.27	0.79	0.67	0.55	0.49
(du/dy) when N=40 (s-1)	11	10	29	22	27	2667	5195	41649
(du/dy) when N=450 (s-1)	122	107	321	250	300	30000	58442	470000
(du/dy)expt.est. (s-1)	230	195	195	53	60	43	200	200

Table 2 - Shear rate for the different Bagnold regimes on FGL heavy mineral spiral

Stream	1	2	3	4	5	6	7	8
D_{50} (μm)	120	215	300	380	495	680	720	560
Vol. Conc.	0.25	0.37	0.42	0.43	0.4	0.3	0.08	0.01
λ^1/2	1.82	2.6	3.09	3.25	2.86	2.05	1.04	0.61
(du/dy) when N=40 (s-1)	571	133	57	34	23	17	30	83
(du/dy) when N=450 (s-1)	6429	1500	643	385	257	190	333	938
(du/dy)expt.est. (s-1)	80	80	125	170	170	69	125	125

The shear rate shown in the last row of the tables is the value estimated from the experimental stream velocity data. By comparing the calculated shear rate with N factor with the shear rate experimentally estimated, the type of interaction can be known. If the experimental estimated value is greater than the shear rate calculated with N=450, then it is grain-inertia regime; If the estimated value is smaller than the shear rate calculated with N=40, then it is macro-viscous regime.

From the data shown in Table 1, it was found that for the LD9 coal spiral, the streams 1 and 2 satisfied the conditions for grain-inertia type interactions, streams 3, 4 and 5 fell in between the two criteria, and stream 6, 7 and 8 fell into the macro-viscous regime. From the data shown in Table 2, it was found that for the FGL heavy mineral spiral, stream 1 and 2 are macro-viscous regime and rest of streams are intermediate regime, none of them are grain-inertia regime. The explanation for the difference in flow regimes between the two spirals appears to lie in the difference of D_{50} and value of solid concentration in each stream (Holtham, 1992a).

A similar analysis will be performed later in this study in order to find out the regime of flow in the spiral.

2.2.5 Secondary Flow

Secondary flow in the spiral concentrator was first mentioned by (Gleeson, 1945), who attributed the concentrating effect of the spiral to a secondary current in the spiral trough. The secondary flow is also called “river bend effect” (Holland-Batt, 1992b), the current is consisting of an outward flow in the top layers of the slurry and an inward flow in the bottom fluid layer close to the trough surface.

in the spiral trough, the fluid at the surface has higher velocity than the fluid at the bottom, while the flow moving around a bend, the top layers will experience a greater inertia or centrifugal force than the bottom layers, as a result, the top layers move outward, which pushing the bottom layers to move inward (Gleeson, 1945). Figure 6 shows schematically the movement of secondary flow inside a spiral trough.

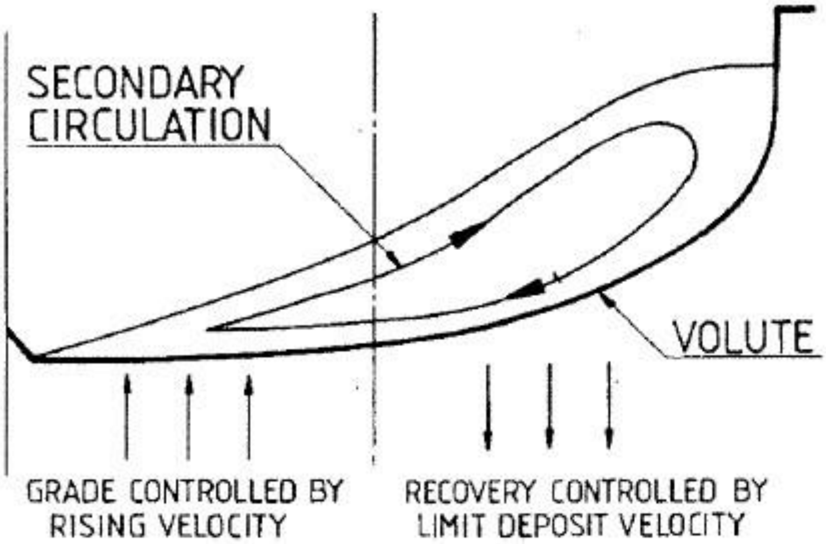

Figure 6 - Secondary flow behavior of spiral concentrator(Holland-Batt, 1987)

As shown in Figure 6, there are rising and falling currents near the inner radius and the outer radius respectively, which move the smaller particles preferentially in contrast to the Bagnold force's preferential lift of the coarser particles (Burt, 1984).

Gleeson (1945) hypothesized that the secondary flow can lift the low density particles to the top layer moving outward and carry them to the tailing streams which is located in the outer zone of the trough; meanwhile, the high density particles settle into the bottom layer of the flow and move inward with the flowing fluid which can concentrate the heavy mineral from the outer streams into the inner streams. However, Gleeson provided only a qualitative explanation to the secondary current theory, but no quantitative analysis was conducted.

Holtham (1990) visualized the secondary flow and conducted a quantitative analysis. He demonstrated the existence of the component of the secondary flow using a dye injection technique, which is shown in Figure 7:

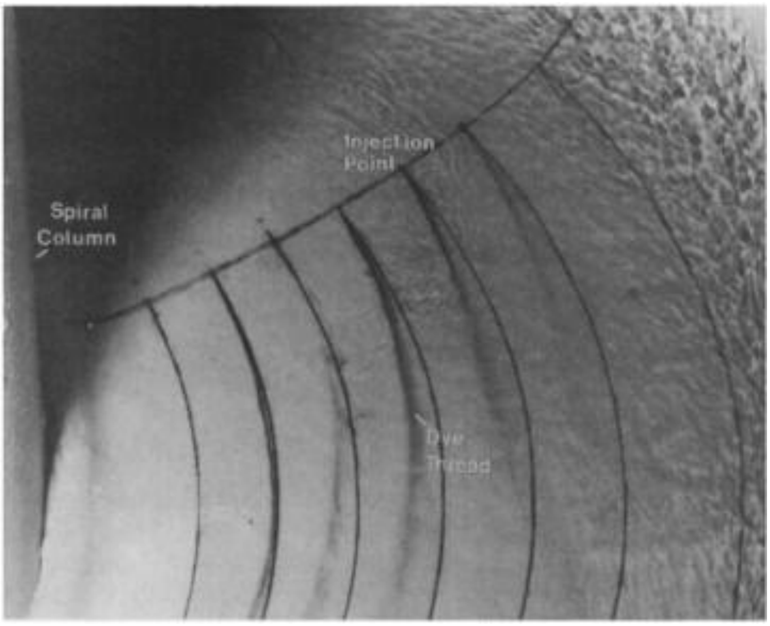

Figure 7 - Secondary flow visualization by dye injection (Holtham, 1990)

As shown in Figure 7, the fluid close to the trough surface experienced inward deviation, this deviation increases as the radial position of the fluid increases. The fluid from the outer part of the trough deflected inwards would reach the inner radius after approximately one and a quarter turns. A remarkable observation of the treating of a rutile-quartz feed shows that the concentrate band becomes clearly established within a similar distance from the feed point, which implies that the secondary flow plays a role in the separation mechanism.

Loveday (1993) also performed a series of tests to demonstrate the existence of the secondary flow in a spiral concentrator. The feed consisted 30% solid w/w, the heavy mineral (chromite) was between 40% and 70%. The spiral employed for the tests was a Multotec spiral having five turns. The main stream was divided into 8 streams at the foot of the spiral with stream 1 being nearest the central column. The grade of chromite of each stream was measured, with data is shown in the following table:

Table 3 - Grade of chromite (percentage by mass) (Loveday, 1993)

chromite % in feed	1	2	3	4	5	6	7	8
40%	98	97	96	98	67	2	0	3
	98	99	95	98	65	3	0	0
	98	99	95	98	66	2	0	0
	98	97	94	98	73	3	0	0
	98	96	95	98	67	2	0	0
70%	99	99	86	96	50	1	1	0
	99	99	88	97	56	2	0	0
	98	99	95	93	49	1	0	0
	99	98	95	66	13	1	0	0
	99	99	87	97	62	1	0	0

As shown in Table 3, the grade of chromite generally decreases as the radial position increases. However, stream 3 for every run exhibits an unusual lower chromite grade compare to the adjacent streams. An explanation for this phenomenon is that the lift point of the circulating secondary current is located at stream 3, thus part of chromite in the stream 3 are lifted to the top layer of the slurry and be transported to the out streams by the secondary flow. In this series of tests, the secondary flow plays a counterproductive role in the heavy mineral concentration.

For a secondary flow to exist, the boundary condition at the slurry surface requires that gravitational and centrifugal forces must be equal as the shear stress is zero at the surface (Holland-Batt, 1987). However, when the radial profile of the trough is too steep, the centrifugal force cannot overcome the gravitational force, as a result, the secondary flow would be absent.

2.3 Profiles of Primary Flow of Spiral Concentrator

In this section, the various types of flow profile that could exist in the spiral concentrator are summarized. These flow types were analyzed in detail by Holland-Batt (1987) in order to figure out the applicability of each flow profile to a spiral concentrator.

2.3.1 Laminar Flow

Laminar flow occurs when a fluid flows in parallel layers with no disruption between the layers (Batchelor, 2000). The shear stress (τ) in laminar flow can be expressed as:

$$\tau = \rho_f\, g\, (h_t - h) \sin\theta \qquad (2.23)$$

Where ρ_f the density of the fluid, g is the gravitational force, h_t is the total depth of the fluid, and θ is the angle of the plane to the horizontal. h is the height at which the shear stress is calculated, therefore, the shear stress(τ_o) at the surface of the plane when $h=0$ is:

$$\tau_o = \rho_f\, g\, h_t \sin\theta \qquad (2.24)$$

The velocity V of the flow is conventionally express as:

$$v = \sqrt{\frac{\tau_o}{\rho_f}} \qquad (2.25)$$

Combining with Equation 2.24, it can be expressed as:

$$v = \sqrt{g\, h_t \sin\theta} \qquad (2.26)$$

For laminar flow, the shear stress is equal to the product of the fluid viscosity μ and the shear rate $\frac{dv}{dh}$, Equating and solving the resulting differential equation, the velocity of the laminar flow can be written as:

$$v = \frac{\rho_f\, g}{2\mu} h\, (2h_t - h) \sin\theta \qquad (2.27)$$

The mean velocity resulting from this profile can be calculated by the following integral: $\bar{v} = \frac{1}{h}\int_0^{h_t} v\,dh$ (2.28)

Substituting Equation 2.27 into 2.28 and solve the integral, the mean velocity $\bar{v}$ of the laminar fluid profile is:

$$\bar{\mathrm{v}} = \frac{\rho_f g {h_t}^2}{3\mu} \sin\theta \qquad (2.29)$$

The volumetric flow rate Q of a flow with a height h_t, a width W and a mean velocity $\bar{\mathrm{v}}$ can be written as:

$$\mathrm{Q} = \bar{\mathrm{v}}\, h_t W \qquad (2.30)$$

Combining Equation 2.29 and 2.30, we can derive the equations for calculating the total height of the flow:

$$h_t = \left[\frac{3\mu Q}{\rho_f\, g \sin\theta W}\right]^{1/3} \qquad (2.31)$$

And the mean velocity of the flow:

$$\bar{\mathrm{v}} = \left(\frac{\rho_f\, g \sin\theta \mathrm{Q}^2}{3\mu W^2}\right)^{1/3} \qquad (2.32)$$

Holland-Batt (1987) used Equation 2.29 to calculate the mean velocity of the flow in the inner zone of the spiral by assuming it is laminar flow, the depth of the flow is 0.2 cm and the slope of the trough is 20 degrees. The result given by Equation 2.29 is 447.2 cm/s, however, the measured flow speed for inner zone flow is approximately 50 cm/s; the calculated value is almost nine times higher than the measured value. Therefore, Holland-Batt concluded that it is not feasible to assume laminar flow the inner zone. Even the flow velocity and the flow height of the inner zone are lowest in the spiral trough.

In the tests conducted by Holtham (1992b), similar calculations were undertaken, with the findings being that the flow profile of the stream depends on the radial position of the flow in the trough. To determine the profile type of the fluid, the Reynolds number for an open channel flow with a liquid must be considered, the Reynolds number during unsteady motion being defined as:

$$\mathrm{Re} = \frac{\bar{\mathrm{v}} \rho_f h_t}{\mu} \qquad (2.33)$$

When Re<400, the fluid is typical laminar flow, and when Re>2000, the fluid motion will become turbulent. The transition from laminar flow to turbulent flow occurs at $400<Re<2000$. Holtham (1992b) then verified the applicability with clear water, the measured flow velocity being 0.2 m/s and a flow height of 1.5 mm on average across the trough. The calculated Reynolds number is 300, thus the flow should be laminar. However, by using the Equation 2.29 taking the slope of the trough as 20 degree, the mean velocity of the flow should be 2.4 m/s, which is much too high as measured value, which confirmed the conclusion of (Holland-Batt, 1987). Therefore, the laminar flow profile is not applicable for fluid in the spiral concentrator, but it might be valid when the viscosities become higher when the clear water is replaced by slurry with a high solid concentration.

2.3.2 Smooth Turbulent Flow

Smooth turbulent flow is another shallow flow regime, in which the viscosity still plays a role, but the roughness of the underlying surface does not affect the main flow (Yalin, 1977). The mean velocity profile $\bar{v}$ is described as follow:

$$\bar{v} = \frac{v}{\kappa}\left(\ln \frac{9\rho h_t v}{\mu} - 1\right) \tag{2.34}$$

v is the shear velocity, which can be calculated with Equation 2.26, when the slope of the spiral trough is 20 degree, the shear velocity v is 8.19 cm/s. κ is the Karman constant, which is assumed to be 0.4. As a result, the mean velocity of the flow is 130 cm/s, which is still higher than the measured value of 50 cm/s, thus the smooth turbulent flow regime is not applicable to the flow in spiral concentrator (Holland-Batt, 1987)

2.3.3 Rough Turbulent Flow

In a rough turbulent flow regime, where the flow viscosity no longer plays any part in regulating the behavior (Yalin, 1977), the mean velocity of rough turbulent flow can be written as:

$$\bar{v} = \frac{v}{\kappa}\left(\ln\frac{30h_t}{k_s} - 1\right) \tag{2.35}$$

where K_s is the roughness height, which for flow over a bed of solids may be described conveniently in terms of the 65% passing size of the solids size distribution (Holland-Batt, 1990), for the experiment conducted by Holland-Batt, it is approximately 0.07 cm. This yielded a mean velocity of 70.65 cm/s, closer to the measured value of 50 cm/s, but still the complexity of the equation made it mathematically inconvenient to use.

2.3.4 The Suspension Flow

The mean velocity of suspension flow profile reported by Holland-Batt (1990) is calculated by the following equation:

$$\bar{v} = \frac{v}{\kappa}\left(\ln\frac{h_t}{35.45k_s} - 1\right) + 17.66 \tag{2.36}$$

when Holland-Batt applied this profile to his experiment, he found that the mean velocity of the flow is 72.59 cm/s which is of the same order as the result obtained for rough flow. According to (Holland-Batt, 1990), if the concentration of solid is significant, the Karman constant should be modified, the predicted mean velocity would be 48.58 cm/s which is in good agreement with the measured value, if the Karman constant is 0.3 instead of 0.4 as assumed previously.

A common drawback of all turbulent flow equations is, when the attempt is made to determine the flow height and mean velocity required to generate a particular volumetric flow rate, a transcendental equation arises that does not permit a direct solution (Holland-Batt, 1987).

2.3.5 The Manning Profile

The manning equation is known as an empirical formula estimating the mean velocity of a fluid flowing in an open channel and is driven by gravity. It is often used to describe non-laminar flow, the standard form of the Manning Equation provides the mean velocity over the total depth, and the relationship can be written as:

$$\bar{v} = k{h_t}^{2/3}\sqrt{\sin\theta} \tag{2.37}$$

where k is the Manning constant, in the empirical model developed by Loveday (1970), he found that on spiral concentrator, the value of k should be approximately 250, thus the mean velocity of the flow on spiral trough in manning profile is 50 cm/s, which agrees well with the observed behavior.

Holland-Batt compared the velocity profiles of various flow profile mentioned above based on the data used in the trial calculations, and the plot is shown in following figure:

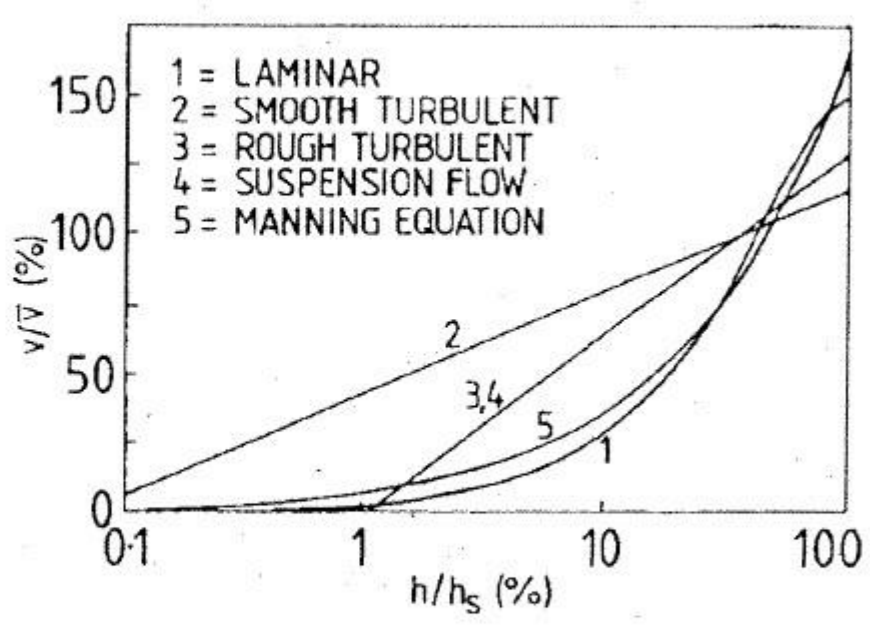

Figure 8 - The velocity profile of the flow on a spiral concentrator summarized by (Holland-Batt, 1987)

The Manning equation provides a velocity profile similar to the laminar curve, rough turbulent and suspension flow yield a coincident curve since they share a common origin, the smooth turbulent displays a different slope from the others, but all three turbulent profiles are linear.

The Manning equation has ability to provide an adequate description of a wide range of non-laminar flow problems, however, this profile does not include a solids concentration term, as discussed previously, solids concentration plays a major role in slurry flow, thus a profile than can describe slurry flow appropriately must take account for particle effect.

2.3.6 The Flow incorporating Particle Effect

Loveday (1993) developed a new method of describing the velocity profile which accounts for the particle effects by considering the Bagnold shear stress. The profile provides a fundamentally based velocity profile which does not rely on empirical correlations. To apply this profile, two conditions must be satisfied: the solids concentration must uniform through the slurry film and the regime of the flow must be the grain-inertia regime defined by Bagnold (1954).

The overall shear stress T can be divided into a fluid viscosity component τ_f and a particle interaction component τ_p:

$$\mathrm{T} = \tau_f + \tau_p \tag{2.38}$$

On an inclined plane, the three components in Equation 2.38 can be defined as:

$$\mathrm{T} = \rho_s g(h_t - h)\sin\theta \tag{2.39}$$

$$\tau_f = \mu_w \frac{dv}{dh} \tag{2.40}$$

$$\tau_p = 0.0128\rho_p(\lambda D)^2\left(\frac{dv}{dh}\right)^2 \tag{2.41}$$

where ρ_s is the density of the particle, μ_w is the viscosity of the water, λ is defined as Equation 2.17, and $\frac{dv}{dh}$ is the term that represents the shear rate. To simplify Equation 2.41, a parameter B can be introduced:

$$B = 0.0128\rho_p(\lambda D)^2 \tag{2.42}$$

then

$$\tau_p = B\left(\frac{dv}{dh}\right)^2 \tag{2.43}$$

Combining Equation 2.39, 2.40 and 2.43 yields

$$\rho_s g(h_t - h)\sin\theta = \mu_w \frac{dv}{dh} + B\left(\frac{dv}{dh}\right)^2 \tag{2.44}$$

Thus the roots of this equation can be expressed as：

$$\frac{dv}{dh} = \frac{-\mu_w + \sqrt{\mu_w{}^2 + 4B\rho_s g(h_t - h)\sin\theta}}{2B} \tag{2.45}$$

one root can be rejected to satisfy the condition that the shear rate $\frac{dv}{dh}$ is zero at h=h$_t$, and by integrating Equation 2.45, the mean velocity profile can be written in the following simplified form:

$$\bar{v} = \frac{2}{5}\left(\frac{\rho_s g\, h_t{}^3 \sin\theta}{B}\right)^{1/2} \tag{2.46}$$

Loveday (1993) compared Equation 2.46 with the Manning profile, and it can be noted that the surface velocity produced by the Manning profile is same as the new profile accounting the particle effect, the slurry height h_t and mean velocity $\bar{v}$ can be derived as functions of the volumetric flowrate:

$$h_t = \left(\frac{5}{2}\right)^{2/5} \left(\frac{B}{\rho_s g \sin\theta}\right)^{1/5} \left(\frac{Q}{w}\right)^{2/5} \tag{2.47}$$

and

$$\bar{v} = \left(\frac{2}{5}\right)^{2/5} \left(\frac{\rho_s g \sin\theta}{B}\right)^{1/5} \left(\frac{Q}{w}\right)^{3/5} \tag{2.48}$$

Then Loveday (1993) verified the new profile with the data collected from his experiments. The trough radius is 14.5 cm, total height of the slurry h_t is 5.5 mm, the volumetric concentration is 0.49, the trough slope is 25.3 degree and the average particles' diameter is 0.55mm which consisted mostly of chromite (specific gravity of 4.49). The mean velocity obtained was 0.42 m/s.

Then Loveday determined the flow regime with the Bagnold number N_B to verify if the conditions of the experiments are satisfied the new profile. As mentioned in Section 2.2.4, if N_B is greater than 450, the grain inertia condition prevails, if it’s less than 40 then the macro viscous conditions prevail, in between these two is an intermediate regime in which the particle interactions are a mixture of the two regimes. The height of the slurry is divided into ten fractions; the shear rate and N_B value of each fraction are shown in the following table:

Table 4 - The shear rate and N_B calculated by (Loveday, 1993)

y	dv/dh	N_B
1	0	0
0.9	67	271
0.8	95	383
0.7	116	469
0.6	134	542
0.5	150	606
0.4	164	664
0.3	177	717
0.2	189	766
0.1	201	813
0	212	857

where $y=h/h_t$, from the table it can be noticed that for majority of the flow height, the conditions to apply the new profile are satisfied, and these fractions located at the bottom of flow they are reasonable to be considered as grain inertia regime.

2.4 Data Interpretation

2.4.1 Mineral Recovery vs. Total Mass Recovery Plots

Holland-Batt (1990) described the following method of data analysis for spiral concentrator tests. The percentage by mass of valuable mineral recovered is plotted against the total mass percentage of solid recovered. Figure 9 shows an example of this plot, the feed grade of the valuable mineral being 40%.

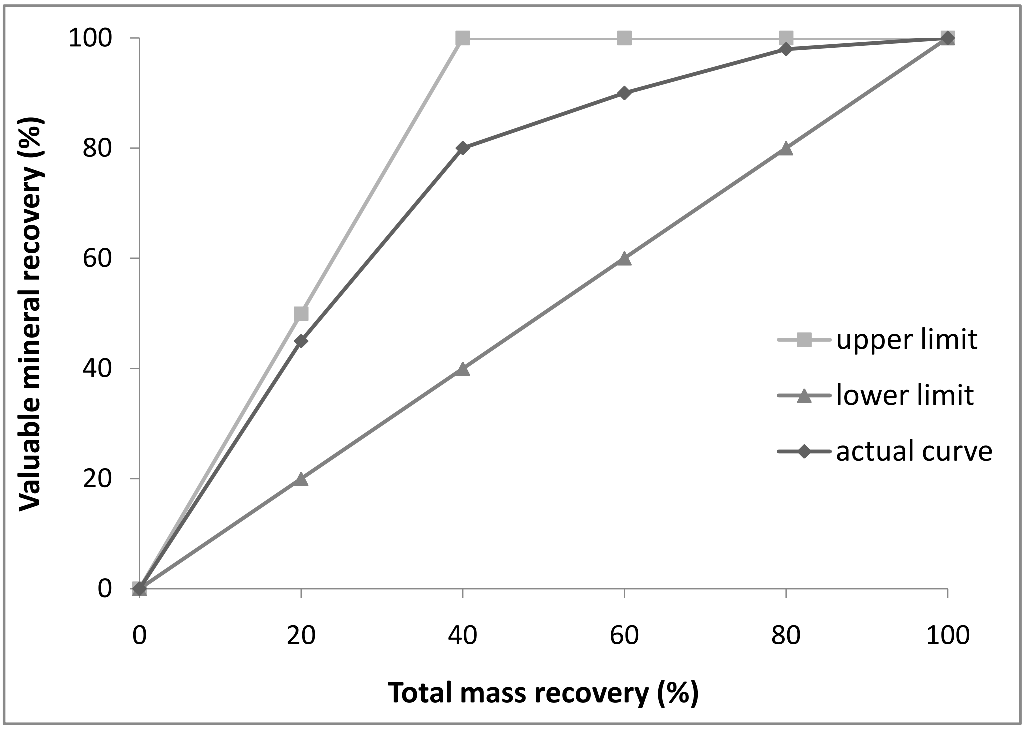

Figure 9 - Example of a mineral recovery vs. total mass recovery

The upper limit is the perfect performance line, which is only an ideal situation. In this situation, the grade of concentrate is 100% until all valuable minerals are being collected, then the gangue starts to add into the concentrate until all material are collected. The lower limit is the line represents zero efficiency, where the grade of the concentrate is always equaled to the grade of the feed, no separation will be observed in this situation.

2.4.2 Efficiency Plots

Holland-Batt (1995) employed efficiency plots to compare the separation efficiency of spirals with different models. The Efficiency E can be calculated with the following equation:

$$E = \frac{R - W}{1 - f} \qquad (2.49)$$

Where R is the percentage of the valuable mineral recovered, W is the total mass percentage of solid recovered, f is the feed grade by mass fraction. An example of an efficiency plot was produced with the same data used in Figure 9, and shown in

Figure 10

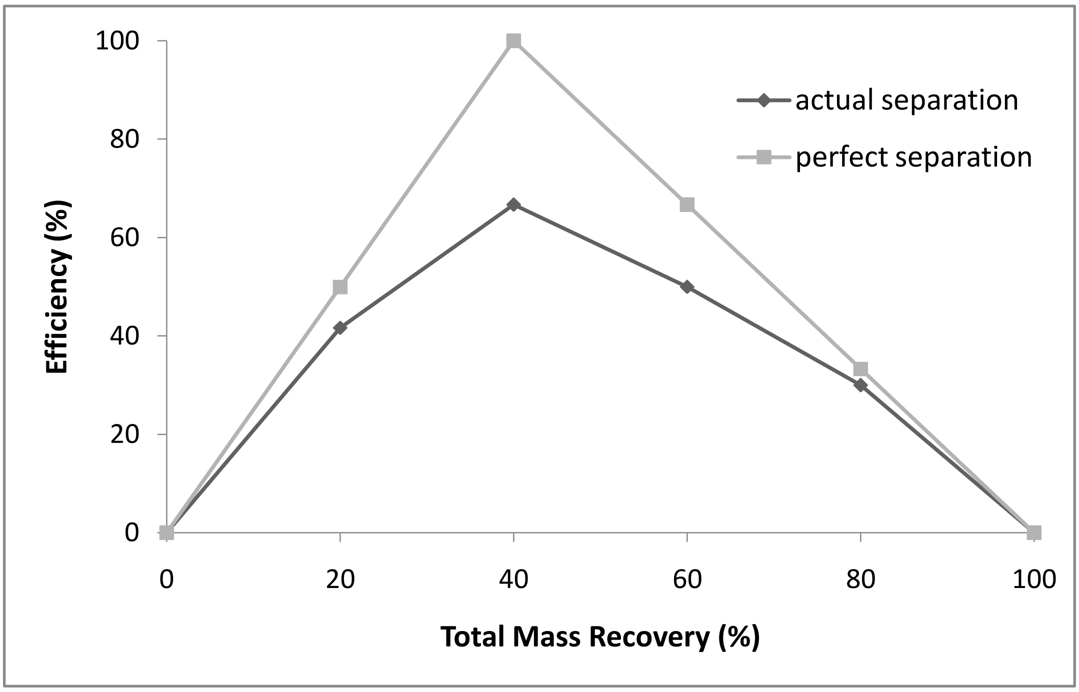

Figure 10 - Example of an efficiency plot

On Figure 10, the curve represents the perfect separation shows that the efficiency of the separation would be 100% at mass recovery=40%, which is the feed grade value. In Chapter 4 of this study, the efficiency plot will be used to compare the separation performance of the spiral at different of turns.

2.4.3 The Upgrade Ratio vs. Total Mass Recovery Plots

Loveday (1993) described the following method of data analysis for spiral concentrator test. The ratio of the concentrate grade to the feed grade is plotted against the total mass percentage recovery, similar to the mineral recovery vs. total recovery plot, the upper limit is the operating line of a perfect separation, and the lower limit is the zero separation. An example of upgrade ratio vs. total mass recovery plot is shown in Figure 11, the data used is same as for Figure 9 and Figure 10.

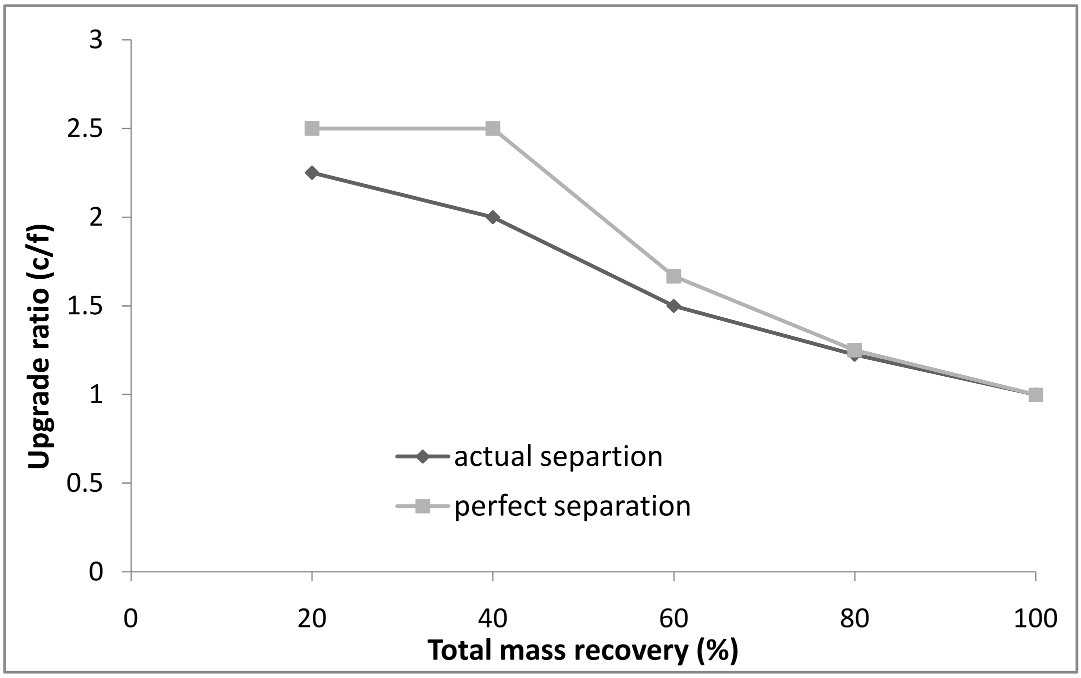

Figure 11 - Example of an Upgrade ratio vs. total mass recovery plot

2.4.4 Partition Curves

The partition functions are widely used in mineral processing analyses. The partition coefficient is the percentage of feed material of a specific density which reports to the concentrate. When the distribution coefficient is plotted against the mean density of the fraction, then a curve is obtained that is called the Tromp Curve or partition curve (Loveday, 1970; Tromp, 1937). Certain characteristics of this curve are used as definitions of separation performance.

King et al. (1992) described the performance of spirals by plotting partition as a function of particle size, which is commonly employed for size separators such as the hydrocyclone.

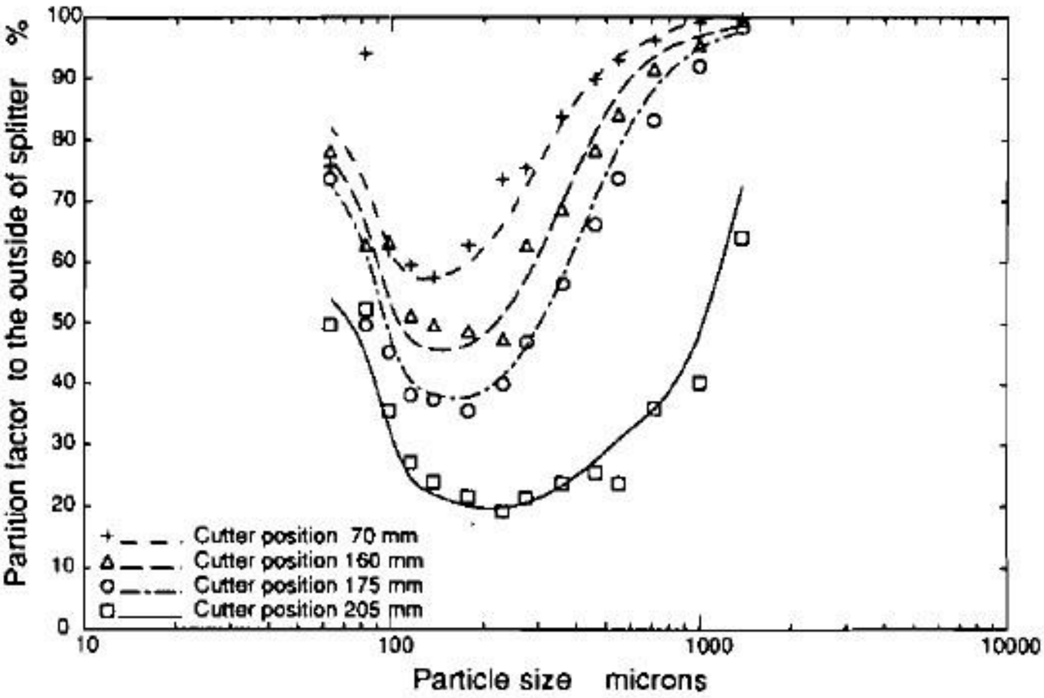

Figure 12 - Measured partition factors as a function of particle size for various splitter positions (King et al., 1992)

The separation process on a spiral preferentially shifts large particles in the particulated bed to the outside of the trough, and some fine particles do not settle into the bed but remain suspended in the water, primarily situated at the outside of the trough. Therefore, the partition curve plotted by King et al. (1992) displays a valley on mid-size range particles, since a majority of the particles in this range report to the inside of the splitter, in other words, they report to the concentrate.

Bazin et al. (2014) made the same observation in their study, and plotted the partition curve of particles reporting to the concentrate as a function of particle size, which is shown in Figure 13

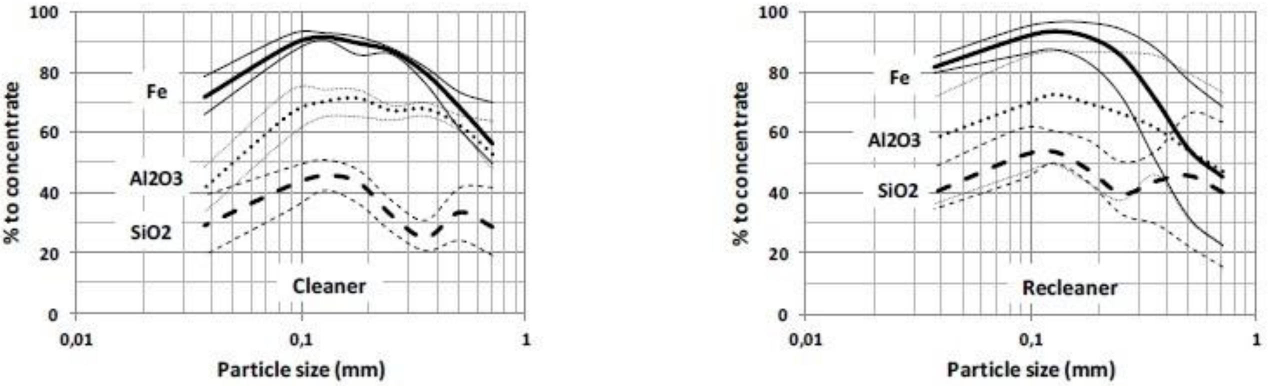

Figure 13 - Partition curves for the spirals of the Lac Bloom concentrator on two different stages (Bazin et al., 2014)

Kelly and Subasinghe (1991) pointed out that the x-axis of the partition function should be the property of the particle which produces the separation. In this study, the partition curves will be based on the function of particle size, which will be shown in detail in Chapter 4.

2.4.5 Comparison of Data Treatments

Each of the treatment described above has its strengths and limitations. The plot of mineral recovery vs. mass recovery can provide a clear picture of the consequences of a change in operating parameter on the recovery of the valuable mineral. However, the concentrate grade is not presented. The upgrade ratio vs. total mass recovery plot can solve the problem mentioned above but suffers from the reverse problem itself, which is missing the data of recovery. Thus, both plots should be used in tandem. The efficiency plot can provide a clear comparison the performance of a spiral with various parameters, such as number of turns or the position of the splitter. Thus in order to appreciate all of the grade, recovery and mass and efficiency, it is necessary to employ all the data treatment methods mentioned.

2.5 Performance Models of Spiral Concentrators

There are a number of models to describe the performance of spiral concentrator have introduced in literature since the invention of this mineral processing device. In general, all the models can be divided into two categories: mathematical models and empirical models.

Mathematical models rely on fundamental physics, which can provide predictions of the forces acting on particles, the flow speed and slurry depth. Due to the complexity of the problem posed by spiral concentrator, the predictions of the performance of the spiral concentrators such as the grade and recovery of the mineral are often done by empirical models. Empirical models require a large number of experiments to determine the empirical parameters of the models, however, compared with mathematical models, the prediction results of the empirical models are usually more precise and more practical for industrial use.

2.5.1 The Holland-Batt Model

Holland-Batt (1987) developed mathematical models of the flow patterns in the spiral concentrator and the cut size of the particle that is theoretically in stasis under the influence of the applied forces and the opposing fluid drag. Holland-Batt then developed mathematical models of the particle deposition velocities in the spiral trough (Holland-Batt, 1992a).

In (Holland-Batt, 1987), the primary and secondary flows were discussed and modeled separately. Moreover, the primary flow was also divided in two regions, an inner region and an outer region. The primary flow velocity profile of the inner region was modeled using the Manning equation, the flow depth was 1 to 3 mm and the mean velocity 50 cm/s. The primary flow velocity profile of the outer region was modeled by the Free Vortex equation. The secondary flow was modeled by numerical techniques in which the centrifugal, gravitational and shear forces were balanced.

To described the behavior of the particles inside spiral trough, (Holland-Batt, 1987) employed following equations:

$$d_r = \left(\frac{18\mu r u}{(\rho_s - \rho_f)v^2(1-C_v)^{4.6}}\right)^{\frac{1}{2}} \tag{2.50}$$

d_r represents the radial cut size of the particle which defines the size of the particle that can just escape outwards driven by the centrifugal force against the opposing liquid flow. μ is the viscosity of the fluid, r is the radial position of the particle, u is the radial velocity component of fluid, ρ_s and ρ_f are the density of solid and fluid respectively, v is the primary velocity component of suspension and C_v is the solids concentration by volume.

The vertical cut size d_h is modeled by the following equation:

$$d_h = \left(\frac{18\mu w}{(\rho_s - \rho_f)g(1-C_v)^{4.6}}\right)^{\frac{1}{2}} \tag{2.51}$$

In Equation 2.51, w is the vertical velocity component of fluid. It is noticeable that the vertical cut size of the particle is irrelevant with the radial position but dependent on the vertical velocity component. Thus Holland-Batt (1992a) developed a model to predict the deposition velocities of the particle based on the original relationship established by Durand (1952). The deposition velocity can be written as

$$V_d = 0.824F_d\sqrt{\frac{8gm(\rho_s - \rho_f)}{\rho_f}} \tag{2.52}$$

0.824 is an empirical number determined by Holland-Batt which represents the ratio between the measured Durand factor $\mathrm{F_m}$ and the predicted Durand factor $\mathrm{F_d}$, the value of $\mathrm{F_d}$ can be manually interpolated with Figure 14.

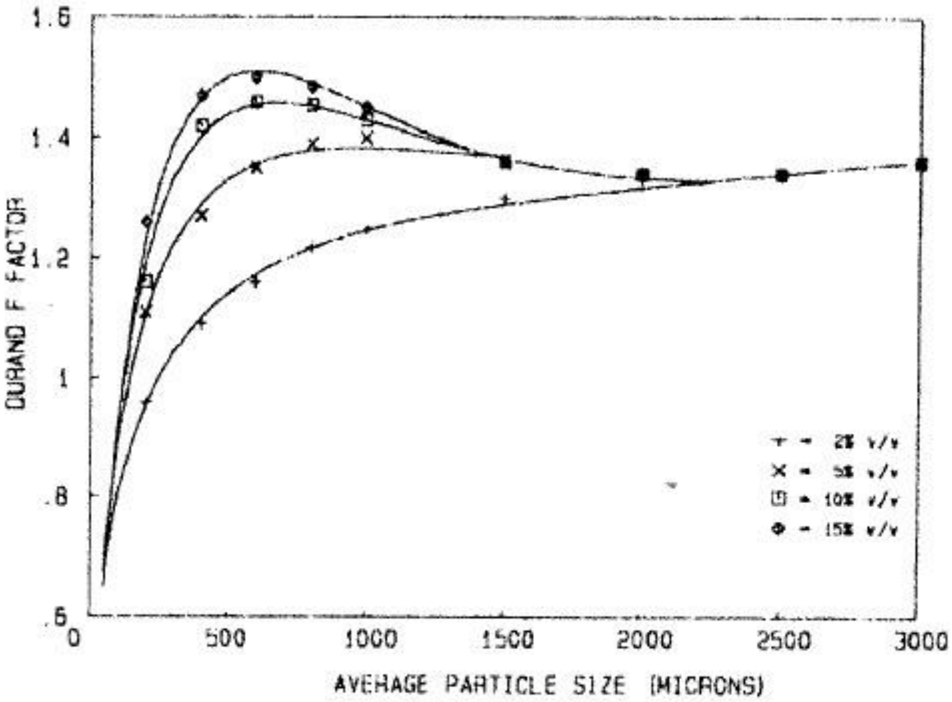

Figure 14 - Durand relationship for F_d (Holland-Batt, 1992a)

The models developed by Holland-Batt can provide the predictions of velocities of the primary and secondary flow, as well as the deposition velocity of the particles. However, with these parameters it is still hard to predict the recovery of the mineral. In order to have the recovery of mineral, a model that can provide the prediction of particle's radial position on the trough is essential.

2.5.2 The Das Model

Das et al. (2007) developed a mathematical model to simulate the particle and flow behavior in a coal-washing spiral. The framework of the model addressed three components of the spiral system, the geometry of the trough of the spiral, the fluid motion along the curvilinear path of the spiral and the principal forces acting on a particle.

In the model of Das et al. (2007), the position of a single particle is determined as a result of equilibrium force balance. Comparing with the model developed by Kapur and Meloy (1999), the lift force in Kapur's model is considered only as a fixed proportion of the drag force under various flow conditions. In Das' model, the Bagnold effect is included in the equilibrium force balance analysis and the force balance equations have been derived for both "particle-inertial" and "macro-viscous" regime.

Figure 15 shows the distribution of the particle size as a function of equilibrium radial position for a series of different relative specific gravity. To have the recovery of mineral of different particles size and specific gravity, estimating the equilibrium radial position of the particle is only the first step. The next step is to model the probability of a particle being found at different radial position across the trough of the spiral concentrator. To build this model, the empirical method is more efficient compared to the mathematical method.

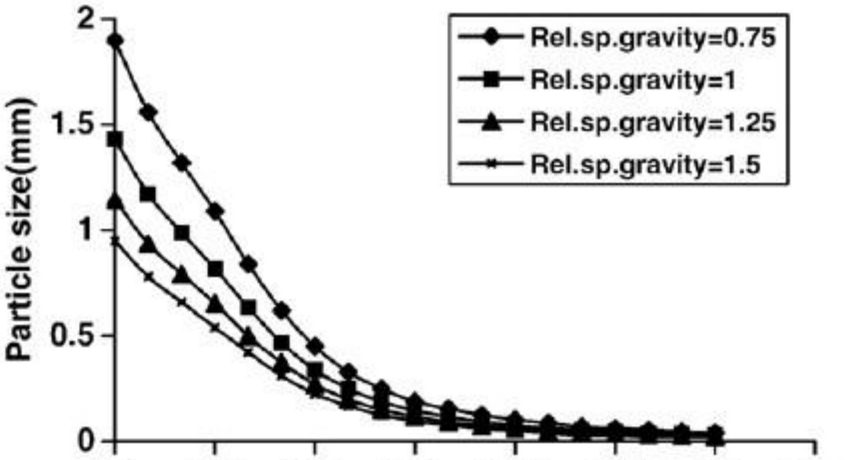

Figure 15 - Effect of relative specific gravity on the radial distribution of particle size (Das et al., 2007)

2.5.3 The Tucker Model

Tucker (1985) developed a model to describe particle distribution profile across the spiral trough. In this model, the spiral bed is divided into two zones, the section between the central column to a radius R_o is called the inner zone, which is approximately 40% of the fractional bed width. The section between a radius R_o to the edge of the trough is called outer zone.

The probability of a particle with a density ρ lying in the inner zone at a radial position R ($R < R_o$) is described by a function of the form:

$$\left(\frac{R}{R_o}\right)^{\alpha} tanh\left[\left(\frac{\rho-1}{b1}\right)^{P1} R\right] \tag{2.53}$$

where $P1$ is the first model parameter, α and $b1$ are scaling factors.

The probability of a particle lying in the outer zone is described by the function:

$$\emptyset = P2exp\left[-\left(\frac{K}{K_o}\right)^{2}\right]\left(\frac{d}{s}\right)^{(p-1/b2)^{-0.15}} + P3\left(\frac{s}{d}\right)^{(p-1/b3)^{-2}} \tag{2.54}$$

where S is the particle size, d is the peak size, here is 125 µm, P2 and P3 are empirical parameters, K is the concentrate port number counted from the top of the spiral and K_o is a scaling factor.

In Equation 2.54, the first term accounts for the fine particles trapped close to the outer radius, which is depending on the distance down the trough. The second term of the equation relates to the proportion of coarse particles whose equilibrium radius lies within the outer radial zone. Therefore, for a given radial position R, the model becomes:

$$x = \frac{\left(\frac{R}{R_o}\right)^{\alpha} tan\,h\left[\left(\frac{\rho-1}{b1}\right)^{P1} R\right]}{\emptyset + tan\,h\left[\left(\frac{\rho-1}{b1}\right)^{P1} R_o\right]} \tag{2.55}$$

Where x represents the probability that material just above concentrate port K leaves the flow stream at that port. This model has successfully predicted the probability of particles with a diameter d and a density ρ certain lying into the inner zone; the next model that will be introduced can predict the recovery of the minerals with various size and density by describing the partition curves.

2.5.4 The Bazin Model

Bazin et al. (2014) proposed an empirical model to solely represent the shape of the partition curves observed for minerals of different density. The shape of the partition curves is close to the bell curve, this is due to the actions of two mechanisms. One mechanism forces the heavy minerals toward the center of the spiral and the other one pushes the coarse particles toward the outer part of the spiral. Therefore, the model used to fit the observed partition curve can be described by:

$$y(d,\rho) = S_c(d,\rho) \times P_R(d,\rho) \tag{2.56}$$

where $y(d,\rho)$ represents the proportion of the particles of size d and density ρ in the spiral feed that reports to the concentrate, i.e. the proportion of the particles recovered. S_c is the proportion of the feed driven by the gravity force and should report to the concentrate; P_R is the proportion of the feed successfully resists an outward force that push the particle toward, and this proportion is finally directed toward the concentrate.

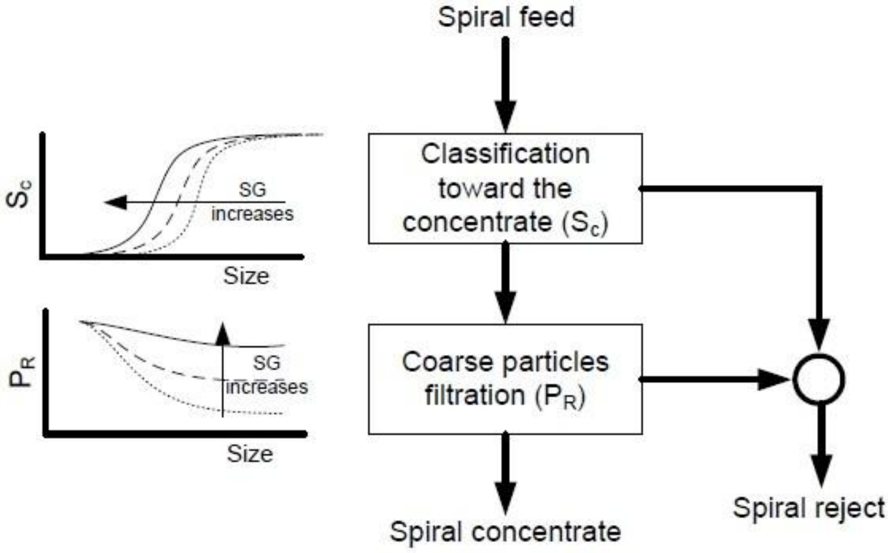

Figure 16 - Structure of the empirical model for a spiral concentrator (Bazin et al., 2014)

As shown in Figure 16, the proportion of the particle that should report to the concentrate due to the gravity force, i.e. S_c , increases with particle size; conversely, the resistance to the outward force, i.e. P_R , deceases with the particle size. Bazin et al. (2014) proposed two equations to describe S_c and P_R respectively:

$$S_c(d,\rho) = \frac{exp\left(\alpha_s(\rho)\frac{d}{d_{50;s(\rho)}}\right)-1}{exp\left(\alpha_s(\rho)\frac{d}{d_{50;s(\rho)}}\right)+exp\left(\alpha_s(\rho)\right)-2} \tag{2.57}$$

$$P_R(d,\rho) = R_P(\rho) + \left(1 - R_P(\rho)\right)\left\{1 - \left[\frac{exp\left(\alpha_P(\rho)\frac{d}{d_{50;P(\rho)}}\right)-1}{exp\left(\alpha_P(\rho)\frac{d}{d_{50;P(\rho)}}\right)+exp\left(\alpha_P(\rho)\right)-2}\right]\right\} \tag{2.58}$$

In Equation 2.57 and 2.58, α_s, α_P, $d_{50;S}$, $d_{50;P}$ and R_P are adjustable model parameters, which are initially assumed to be dependent oo the mineral density. In this model, the α_s and α_P are the parameters to characterize the slope of S_c and P_R curves. The $d_{50;S}$ represents the size of the particles that are equally report to the concentrate and reject to the tailing by the classification action of the spiral. The $d_{50;P}$ represents the size of particles that have 50% chance to be rejected to the tailing due to outward forces, such as the centrifugal force and Bagnold force.

This model was developed for spirals with different feeding conditions in various stages of mineral processing. In the later work of this study, the model will be applied to fit the partition curves on different turns of the spiral and to predict the performance of the spiral with more number of turns.

Chapter 3- Experimental Procedure

3.1 Sample Preparation

A synthetic ore was prepared to mimic a real sample of iron ore from Mont-Wright (Quebec, Canada) which consists mainly of hematite (Fe_2O_3) and quartz (SiO_2), supplied by ArcelorMittal Exploitation Minière Canada, Fermont, Qc, Canada.

The synthetic ore is a binary ore consisting of magnetite (Fe_3O_4) and quartz (SiO_2). In order to facilitate the heavy mineral grade analysis, magnetite was chosen to replace the hematite in the real ore as the heavy mineral in the synthetic ore. Magnetite (SG=5.17) has a similar specific gravity to hematite (SG=5.26), and can be easily separated from the quartz by use of a hand magnet.

In this step, all particles are sized 100% smaller than 850 µm in order to prevent the potential pump blockage during the experiment. Figure 17 shows the particle size distribution of the sample that used as a target for the synthetic ore preparation.

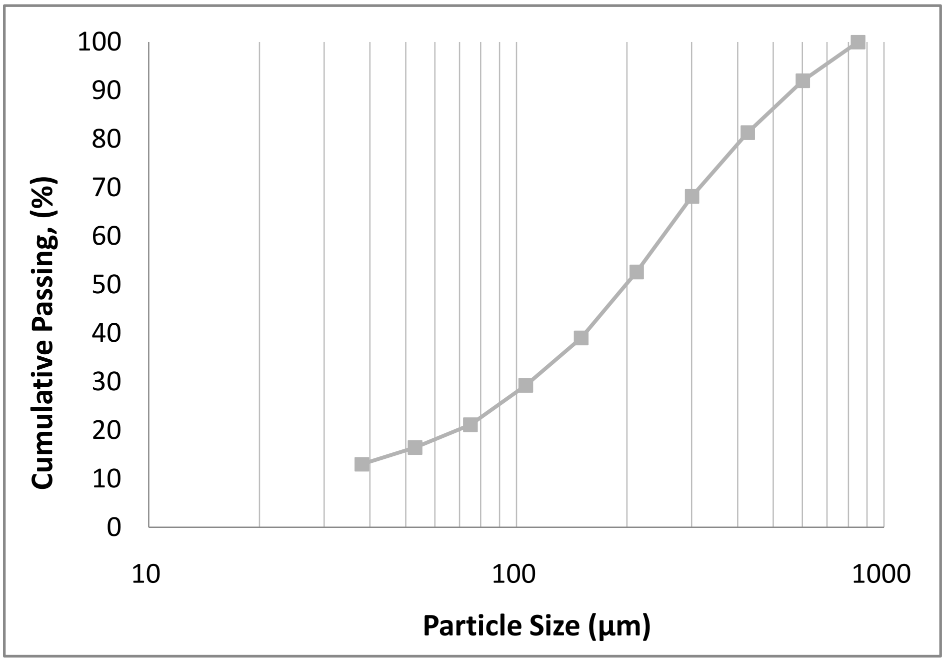

Figure 17 - Size distribution of the iron ore sample from Mont-Wright.

In the real ore, the general grade of hematite is 40.9%; however, the grade of hematite for every size fraction is different. Figure 18 shows the hematite grade in each particle size fraction.

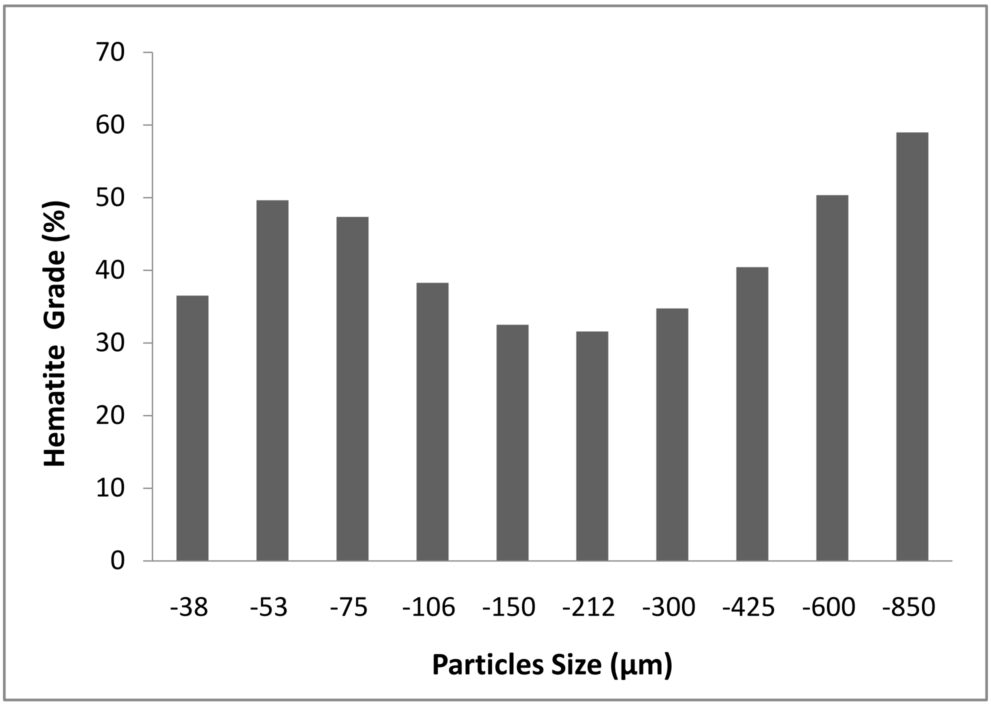

Figure 18 - The grade of hematite of all particle size fractions of the iron ore sample from Mont-Wright

The particle size distribution and the grade of heavy mineral of the synthetic ore are duplicates of the real ore.

3.2 The Closed Loop Experimental Set-Up

The spiral used in this study is WALKABOUT (PW1) spiral concentrator, which has 4 turns with high wear resistant PU trough surface, the height of the spiral is 1000 mm and the diameter is 360 cm, no wash water was used.

Figure 19 - The WALKABOUT PW1 spiral concentrator

The feed of the spiral was prepared in the mixing tank located under the spiral; 4.5 kg synthetic ore was mixed with 18 kg water to form a slurry with 20% w/w solid. A 600 RPM rotating speed mixer was placed at the bottom of the mixing tank to prevent the solid blockage and to minimize the preferential settling of the heavy minerals.

The slurry was transported by a diaphragm pump (Ingersoll Rand Industrial Technologies) from the mixing tank to a funnel located on top of the spiral; such that the funnel reduced the vibration caused by the diaphragm pump to the spiral concentrator, in order to operate under more stable condition, i.e. no vibration. The slurry entered the spiral from the funnel and exited the spiral to the tank, which made the system as a close loop circulating system. Figure 20 shows the schematic sketch of the experimental set-up.

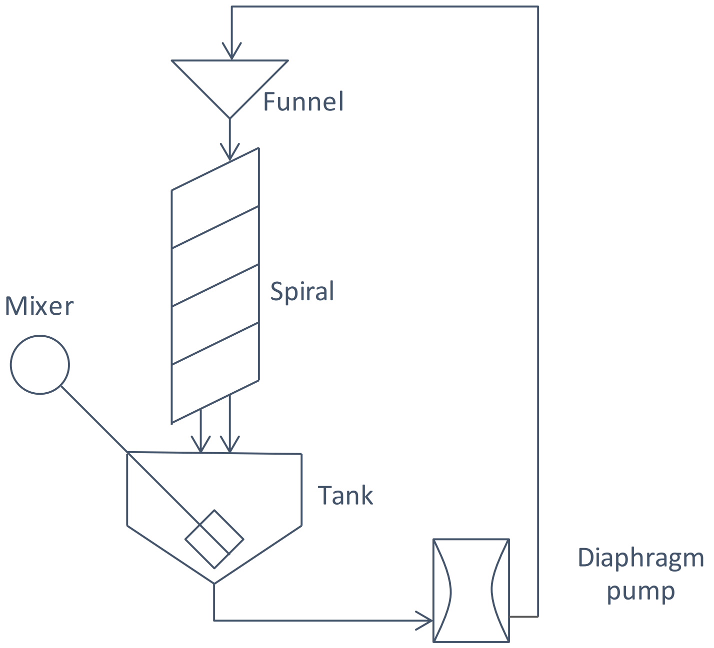

Figure 20 - Schematic sketch of the experimental set-up

3.3 Slurry Splitting and Collection

One of the objectives of this study was to investigate the particle distribution across the spiral trough. In order to analyse the particles in the slurry travelling inside the spiral concentrator, the slurry was collected in 4 different points in the spiral, the collection points were chosen to be at the same location in every turn of the spiral, as shown in Figure 21 (a). At each collection location, the slurry was divided to 4 streams across the trough of spiral. The width of each stream was based on the previous study result with the same model of spiral concentrator (Boucher et al., 2014) The inner stream was termed C1 channel; the middle stream was divided equally to two channels, namely C2 and C3 channels; and the outer stream or the tailing stream was termed T channel. Figure 21 (b) shows the division of slurry stream and the widths of channels.

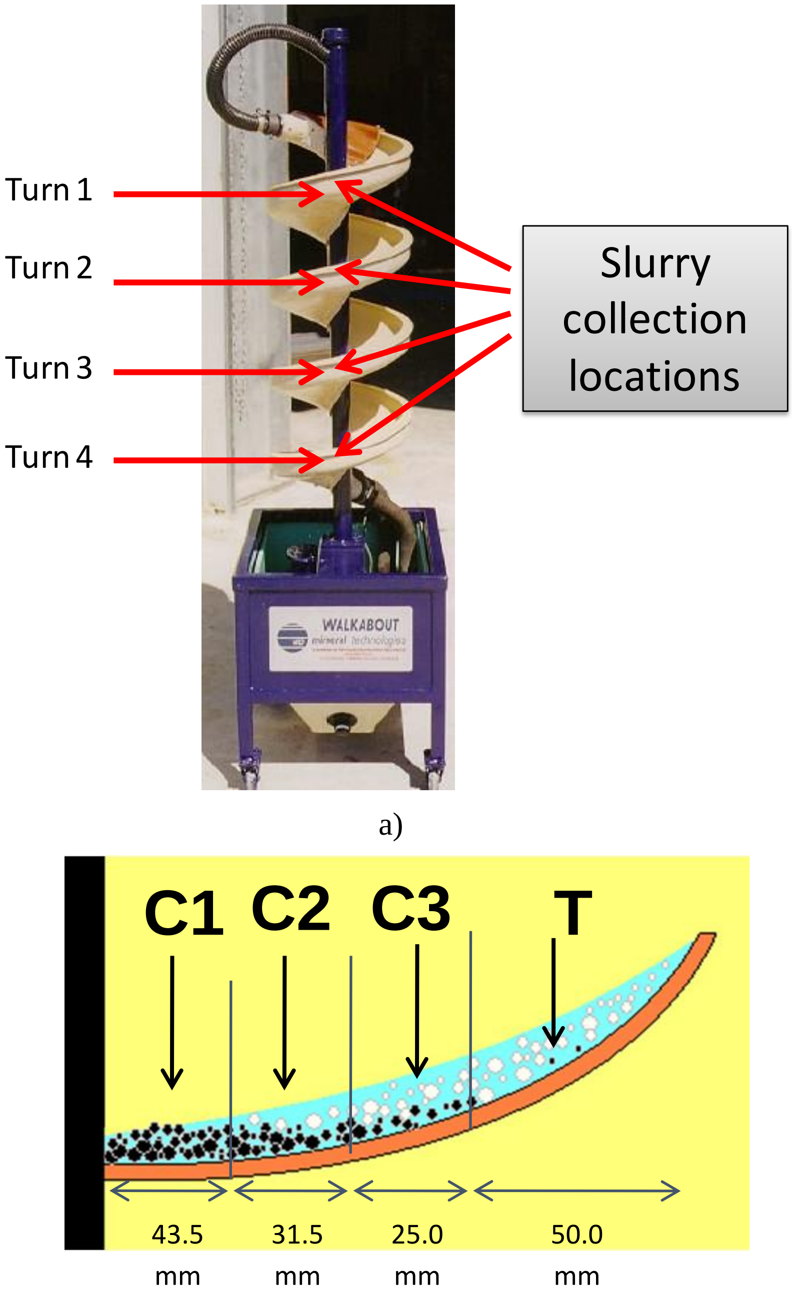

b)

Figure 21 - a) slurry sampling locations in spiral b) cross-sectional view of the trough of spiral

In order to perform the slurry collections, two slurry collectors were designed and made with hand-moldable plastics. Collector A is designed to sample the slurry from inner and middle channels; and Collector B is designed to sample the slurry from T channel.

As shown in Figure 22 (a), Collector A was a container with 3 channels; the width of each channel is equal to C1, C2 and C3 respectively. The base of this container has the same profile with the trough of spiral; Figure 22 b) shows the curve of the base of Collector A.

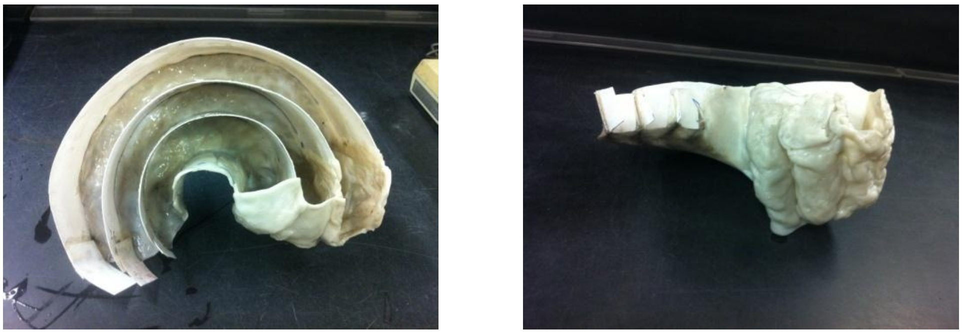

a) b)

Figure 22 - a) Top view of Collector A b) Side view of Collector A

Before sampling the slurry from C1 to C3 channels, the system had to operate for at least 1 minute to reach a steady state. To collect the slurry, Collector A was placed inside the trough of spiral at the position shown in Figure 21 (a), the center of the collector was connected with the central column of the spiral in order to ensure the radial position of the channel openings of the collector are matched with C1, C2 and C3 channels. The next step was pushing the collector into the slurry, and took a 15 seconds sampling. In the end, the collector containing the slurry was removed from the spiral trough.

As shown in Figure 23, Collector B for the sampling of slurry from T channel has a different but simpler structure; it has a hand-moldable plastic made splitter which was connected with a long tube. To sample the slurry from T channel, Collector B (both splitter and tube) had be to placed inside the trough before the system started to operate; and the gap between the collector and trough was sealed with plastic tape. The next step was running the system, the slurry of the tailing stream was passing through the collector B, once the system reached the steady state, the slurry sample was collected by bring the tube of Collector B to the outside of the trough and connected to a bucket, the sampling time was 15 seconds.

Figure 23 - Collector B for sampling the slurry from T channel

For the slurry sampling with both collectors, a fresh feed to the system had to be prepared prior to the start of sampling in order to maintain constant initial conditions. The slurry sampling was been performed 3 times at every turn of the spiral from the 1st turn to the 4th turn, and the slurry from each channel of every turn was analyzed separately.

3.4 Slurry Analysis

The first step of the analysis was to weigh the slurry from each channel. Then the weight of liquid and solid parts were calculated after size analysis using screens. After the screening, the solids are classified into 10 size fractions from -38 µm to -850 µm. A magnetic separation was been performed for each size fraction, the weight of magnetite and quartz in the size fraction were recorded. At the end of this investigation, the size distribution of the particles and the grade of magnetite for each channel and each turn of the spiral were mapped.

3.5 The Profile Gauge

The profile gauge (Figure 24) used in this study to measure the profile of trough or slurry surface is developed from the one used by Holland-Batt (1987), and Loveday (1993) conducted his experiment using the similar gauge. The body of the gauge consisted of a wooden arm through which a series of holes were drilled vertically. Nine threaded screws passed through these holes which could be raised or lowered to contact the trough or slurry surface. The arm projected radially from the centre column of the spiral with one end attaching to the centre column and another end resting on the edge of the trough.

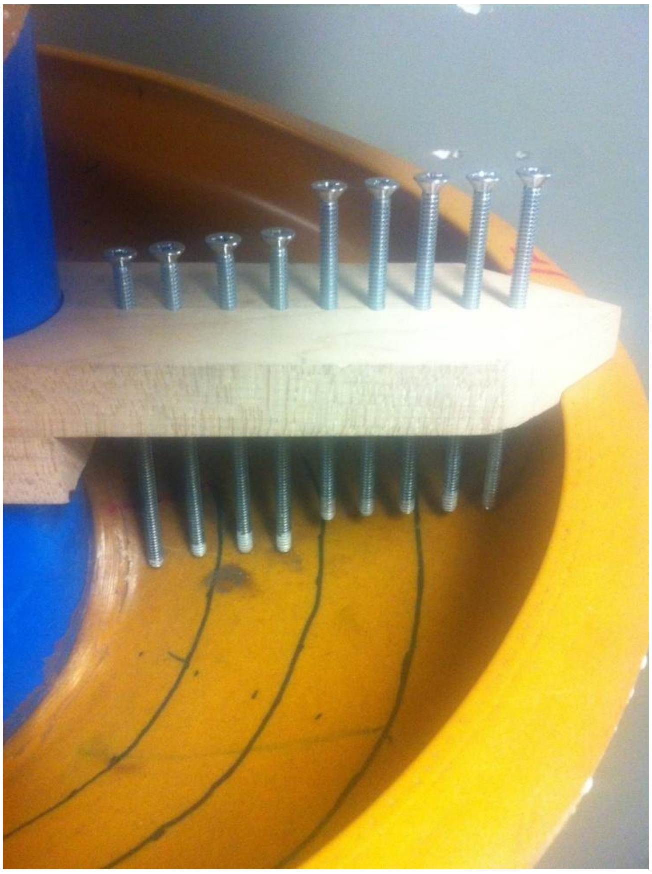

Figure 24 - The profile gauge

3.6 Profile Measurement

Prior the start of experimental process, the profile of the trough at the slurry collection points were measured by turning the screws until the ends were touching the surface, the profile of slurry surface can be measured with the same method. The flow heights could be calculated as the difference between the trough profile and the slurry profile.

Chapter 4 - Results and Discussion

4.1 Flow Rate

The mass flow rates can be measured directly, which are shown in the following table:

Table 5 - The mass flow rate of solid and water (g/s)

Solid flow	C1	C2	C3	T
Turn 1	3.5	17.4	7.1	12.6
Turn 2	6.6	29.9	11.9	6.6
Turn 3	9.6	22.1	10.9	8
Turn 4	12.3	19.5	6.8	6.8

water flow	C1	C2	C3	T
Turn 1	8.1	17.1	8.9	128.3
Turn 2	3.1	14.3	16.1	121.9
Turn 3	3.3	10	8.1	134.8
Turn 4	3.3	7.9	9	139.9

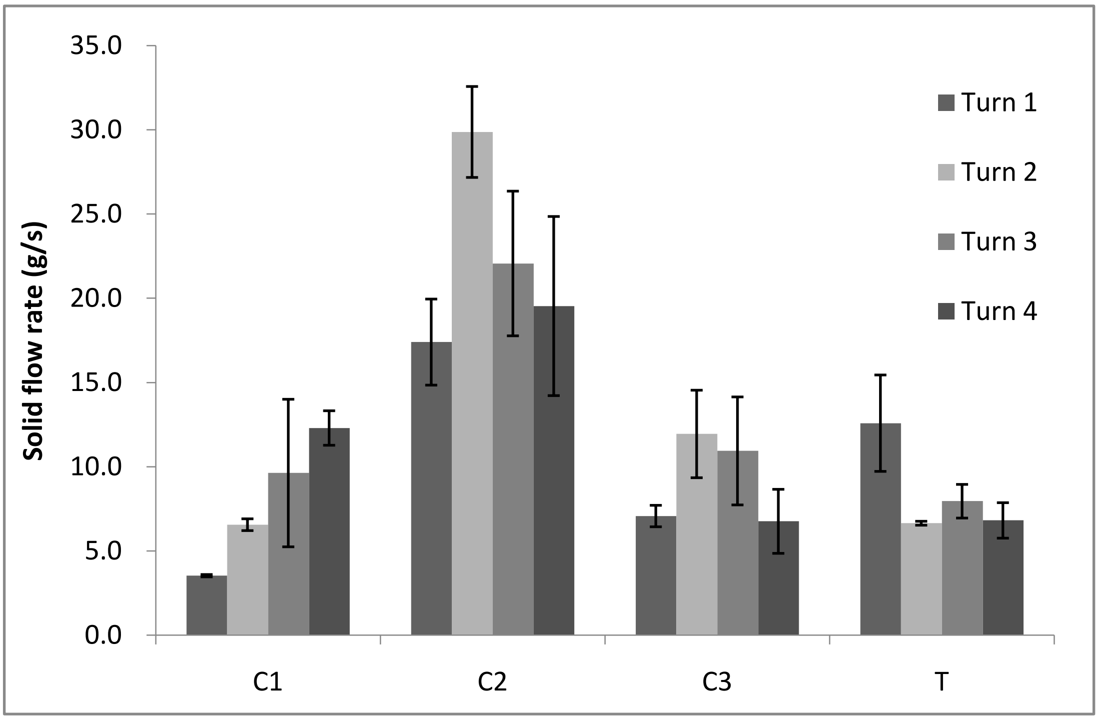

Figure 25 - The mass flow of solids

Figure 25 shows the mean value of the mass flow rate of solids in every channel and every turn. The error bars represent the standard deviations of the measurements. The solids mass flow rate of C1 channel increases regularly from Turn 1 to Turn 4. A reverse situation can be observed in C2 and C3 channels; in these two channels, the solids mass flow rate increases from the Turn 1 to the Turn 2, but decreases gradually from Turn 2 to the Turn 4. The solids mass flow rate of the tailing channel shows a unique trend compared to others channel, it decreases almost to the half quantity from Turn 1 to Turn 2, then since Turn 2 to the end, the quantity of the solid remain roughly same.

Since this is a closed loop system, the total solids mass flow rate in the trough is always same at every turn, (the slight deviation of the total flow rate from turn to turn is caused by the sampling timing changing, which is approximately 0.5). The change of flow rate in an individual channel shows the mass migration between the channels in the spiral concentrator. The observation made from Figure 26 indicates that solid migrates from the middle zone and the outer zone to the inner zone.

Figure 26 shows the average value of the mass flow rate change in each channel for water. The error bars represent the standard deviations of the measurements. It can be seen that the direction of liquid migration is opposite to the solid migration, the majority of the water reports to the tailing stream after Turn 1, and the decrease in water in C1, C2 and C3 indicates that the water moves from the inner zone and middle zone to the outer zone during the separation process in spiral concentrator.

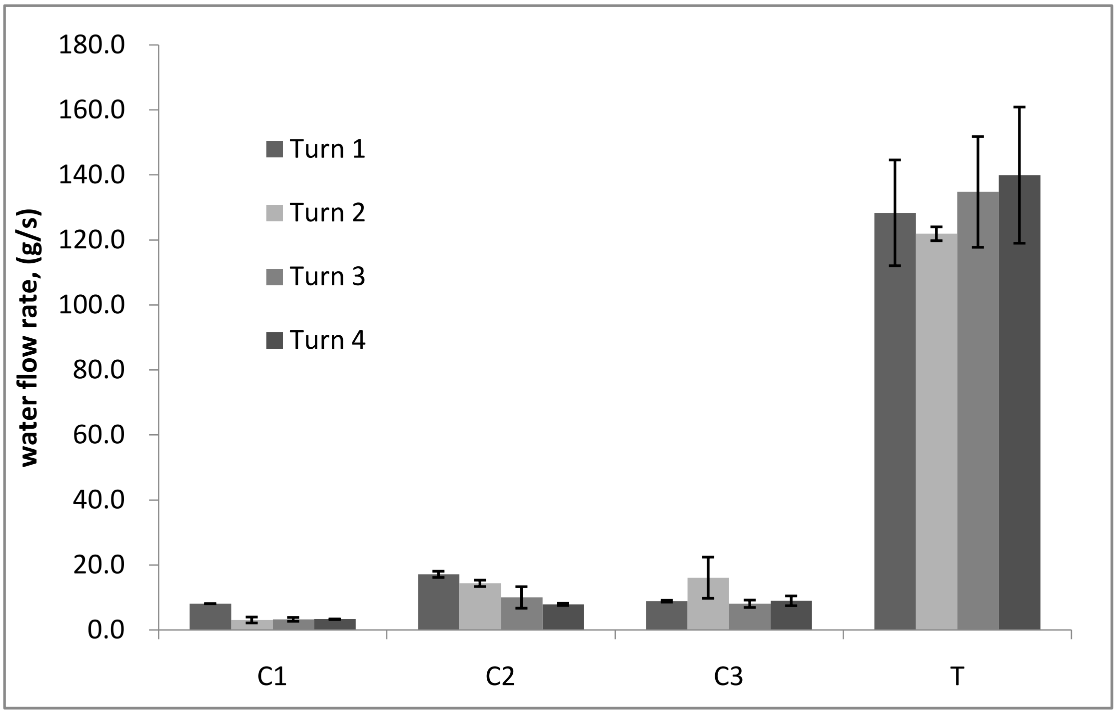

Figure 26 - The flow rate of each channel in each turn of the spiral

In order to calculate the flow speed, the mass flow rate must be converted to the volumetric flow rate. The volume of solids in the slurry can be easily calculated from the measured mass of solid, in this step, magnetite and quartz are treated separately; and then the volume of slurry will be the sum of solid part and liquid part, the volumetric flow rate of the slurry in each channel is shown as follow:

Table 6 - The volumetric flow rate of the slurry (cm^3/s)

	C1	C2	C3	T
Turn 1	9	21.9	11.1	132.5
Turn 2	4.6	22.5	20.4	124
Turn 3	6	16.1	11.4	137.4
Turn 4	5.9	13.9	11.5	142.1

The data shown in Table 6 will be used to calculate the flow speed of the slurry in the spiral trough.

4.2 Flow Height

The profiles of the trough at four slurry collection point are shown in Figure 27. The trough was made out of polyurethane; it is hard to control the shape of the trough to be exactly consistent for every turn. The deviations of the profiles are less than 1mm; the effect of these profile deviations on the slurry flow profile can be neglected.

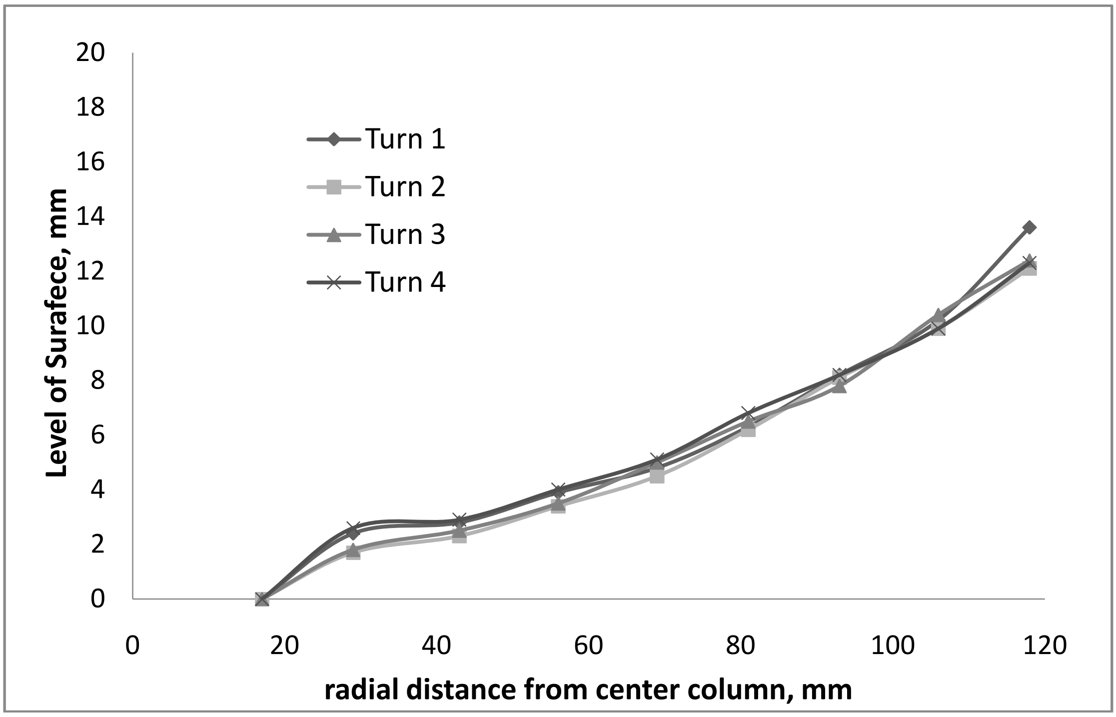

Figure 27 - The profiles of the trough

The flow height measurement was been performed at least 3 times at each point. Figure 28 shows the average value of the flow height for every turn. From the graph, it can be noticed that, at Turn 1, a slurry bump is located on the trough at 45 mm away from the centre column; however, the flow profile becomes smoother as the slurry travels inside the trough, and the height of flow decreases as the number of turns increases. In this closed loop system, the flow rate of the slurry at any point inside the spiral trough should be constant, thus a plausible explanation for this observation is, the flow is accelerated in the trough under the gravitational force, since the volume of the slurry passing through is constant, thus as the flow speed getting higher, the cross sectional area of the flow will be smaller.

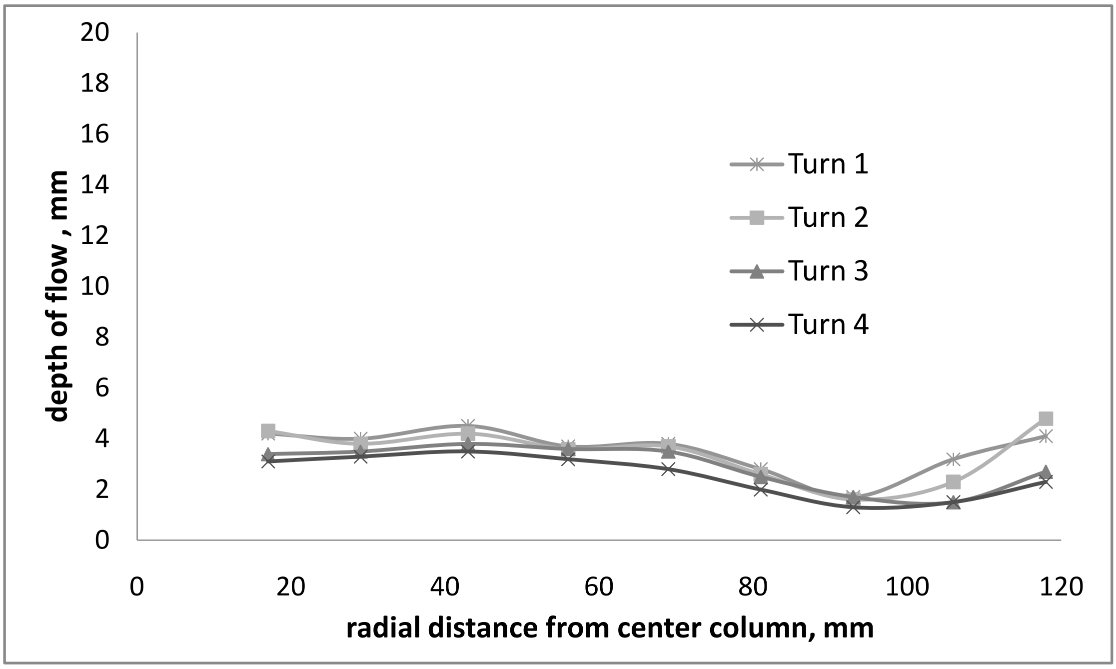

Figure 28 - The flow heights

Figure 28 shows the average flow height in different and turns, the flow height will be used in the next section to estimate the flow speed.

Table 7 - The mean flow height in different channels and turns (mm)

	C1	C2	C3	T
Turn 1	4.10	4.10	2.25	3.00
Turn 2	4.05	3.90	2.10	2.90
Turn 3	3.45	3.70	2.10	1.97
Turn 4	3.20	3.35	1.65	1.70

4.3 Flow Speed

The real cross section of the flow is irregular and complex, in this study, in order to estimate the flow speed, the cross section of the flow in each channel will be simply considered as a rectangular. Table 8 shows the cross sectional area of the flow in each channel:

Table 8 - The mean cross sectional area of the flow (cm^2)

	C1	C2	C3	T
Turn 1	1.066	1.312	0.563	1.200
Turn 2	1.053	1.248	0.525	1.160
Turn 3	0.897	1.184	0.525	0.787
Turn 4	0.832	1.072	0.413	0.680

Table 9 - The velocity of the flow (cm/s)

	C1	C2	C3	T
Turn 1	8.5	16.7	19.8	110.4
Turn 2	4.3	18	38.8	106.9
Turn 3	6.7	13.6	21.8	174.6
Turn 4	7.1	13	27.8	209

The flow speed shown in Table 9 is close to the result obtained by Holtham (1992a) for FLG heavy mineral spiral. The next step is to determine the viscosity of the slurry.

4.4 Physical Properties of the Slurry

As mentioned in section 2.2.2, the viscosity of the slurry is depended on the volume fraction of the solid; the following table shows the w/w % of the quartz and magnetite in each channel:

Table 10 - The weight fraction of the magnetite, quartz and water in the slurry

magnetite %	C1	C2	C3	T
Turn 1	18.3	28	13.3	2.3
Turn 2	56.2	38.7	4.4	1.9
Turn 3	69.7	33.1	2.7	1.5
Turn 4	70.5	26.7	1.8	1.4

quartz %	C1	C2	C3	T
Turn 1	12.1	22.4	31.2	6.6
Turn 2	11.9	28.8	38.2	3.3
Turn 3	10	34.7	50.6	4
Turn 4	8.4	44.6	41.2	3.2

water %	C1	C2	C3	T
Turn 1	69.5	49.6	55.6	91.1
Turn 2	31.9	32.4	57.4	94.8
Turn 3	20.2	32.2	46.7	94.4
Turn 4	21.2	28.7	57	95.4

Since the grade of magnetite is not constant in each channel, therefore the solid density of in each channel is also different:

Table 11 - The density of solid in each channel (g/cm^3)

	C1	C2	C3	T
Turn 1	3.75	3.64	3.1	3.03
Turn 2	4.43	3.68	2.79	3.23
Turn 3	4.62	3.48	2.72	3.06
Turn 4	4.7	3.24	2.7	3.12

By converting the weight fraction to volume fraction, the density of the slurry in each channel can be obtained:

Table 12 - The density of the slurry in each channel (g/cm^3)

	C1	C2	C3	T
Turn 1	1.29	1.58	1.43	1.06
Turn 2	2.12	1.97	1.38	1.04
Turn 3	2.67	1.93	1.51	1.04
Turn 4	2.64	1.97	1.37	1.03

And finally, the viscosity of the slurry can be calculated from Equation 2.5:

Table 13 - The viscosity of the slurry in each channel (mPa s)

	C1	C2	C3	T
Turn 1	1.39	2.13	2.02	1.09
Turn 2	3.48	4.32	2.06	1.05
Turn 3	10	4.81	2.99	1.05
Turn 4	8.3	7.66	2.12	1.04

From the data shown above, one notices that the viscosity of the slurry in C1, C2 and C3 share an increasing trend, but the viscosity of the slurry in T channel decreases with the increasing of number of turns. The viscosity of the feed slurry is 1.23 mPa s, but after the first turn of concentrating, the viscosity of the slurry in C1,C2 and C3 channel is greater than the original viscosity, especially for the C2 and C3 channel. However, the viscosity of the slurry in 1 channel has the largest increment, which indicates that the majority of the heavy minerals are reported into this channel.

4.5 Performance and Efficiency

Figure 29 shows the performance curve of the spiral, as discussed in Section 2.4.1, the upper limit curve represents the perfect separation and the lower limit curve represents the situation with no separation. From the graph one can see that, the separation or the concentration effect starts after Turn 1, and as the number of turns increases, the performance of the separation is getting improved, the performance of the separation in Turn 4 is closest to the upper limit.

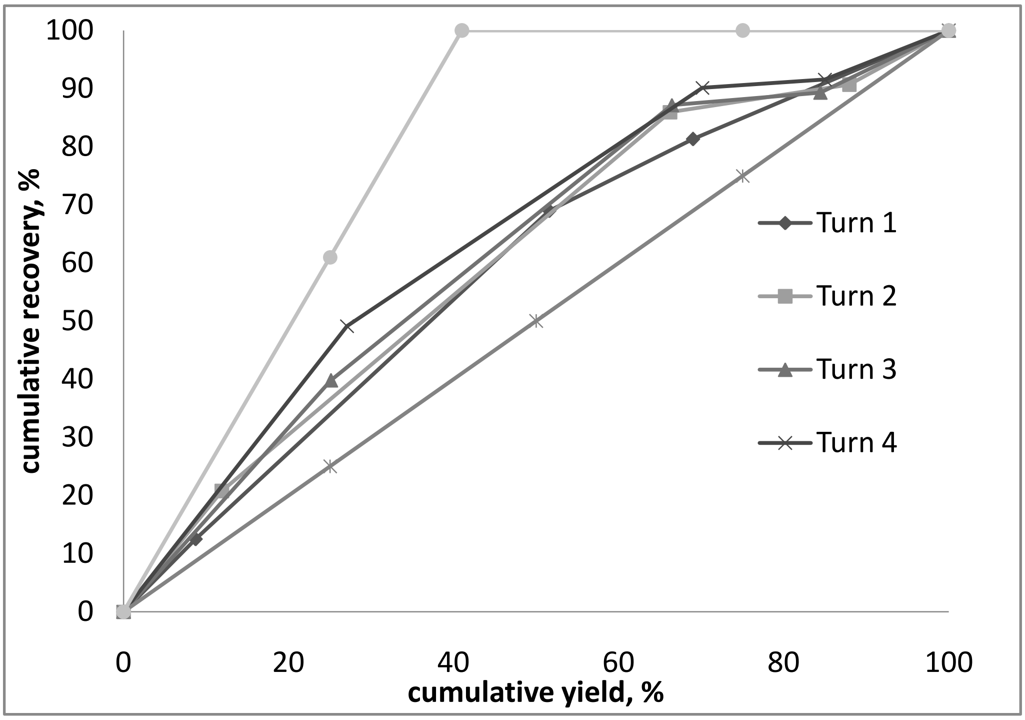

Figure 29 - Mineral recovery vs. total mass recovery

The efficiency plot of the spiral concentrator is shown in Figure 30, compare the efficiency curves, the separation efficiency in Turn 4 is highest among all turns. The general trend of efficiency change is that the efficiency enhanced when the number of turns increased.

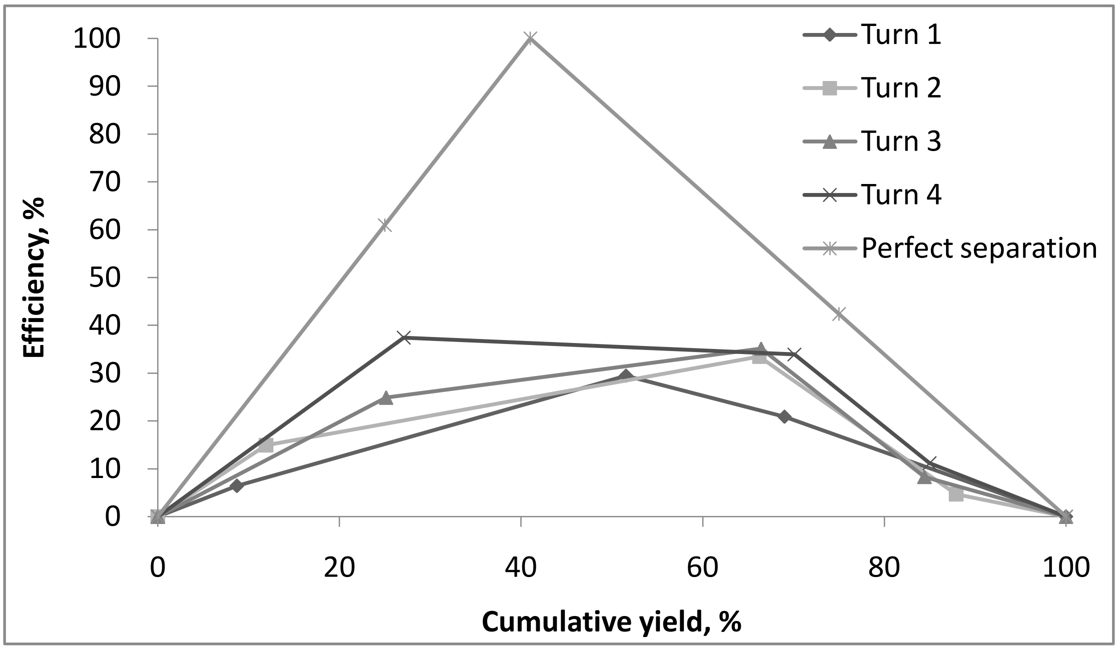

Figure 30 - The efficiency of the separation

4.6 Mineral Recovery vs. Concentrate Grade Plots

The Mineral Recovery vs. Total Mass Recovery Plots can only present the recovery of mineral, however, the grade of concentrate is another important parameter required to be considered. Therefore, to present both the recovery and concentrate grade at same time, the recovery vs. concentrate grade plot has to be employed,

Figure 31 shows the recovery of the magnetite in every channel as the number of the turn changes. The recovery of magnetite in channel x is noted as $R_{m;x}$ and is calculated using:

$$R_{m;x} = \frac{W_{m;x}}{W_{m;T}} \tag{4.1}$$

The variable $W_{m;x}$ represents the weight of magnetite reported to channel x, and $W_{m;T}$ represents the total weight of magnetite collected from all 4 channels.

As the number of turn increases, the magnetite recovered in C1 channel increases constantly. In C2 channel, the recovery of magnetite increases from Turn 1 to Turn 2 while the recovered magnetite drops in C3 and T channel. However, from Turn 2 to the Turn 4, the magnetite recoveries in C3 and T channel stay almost at a constant level, but decreases gradually in C2 channel. These observations indicate that, at Turn 1 of the process, magnetite migrates from the outer zone to the mid zone; however, from Turn 2 to the last turn, the major migration of the magnetite occurred from the middle zone to the inner zone.

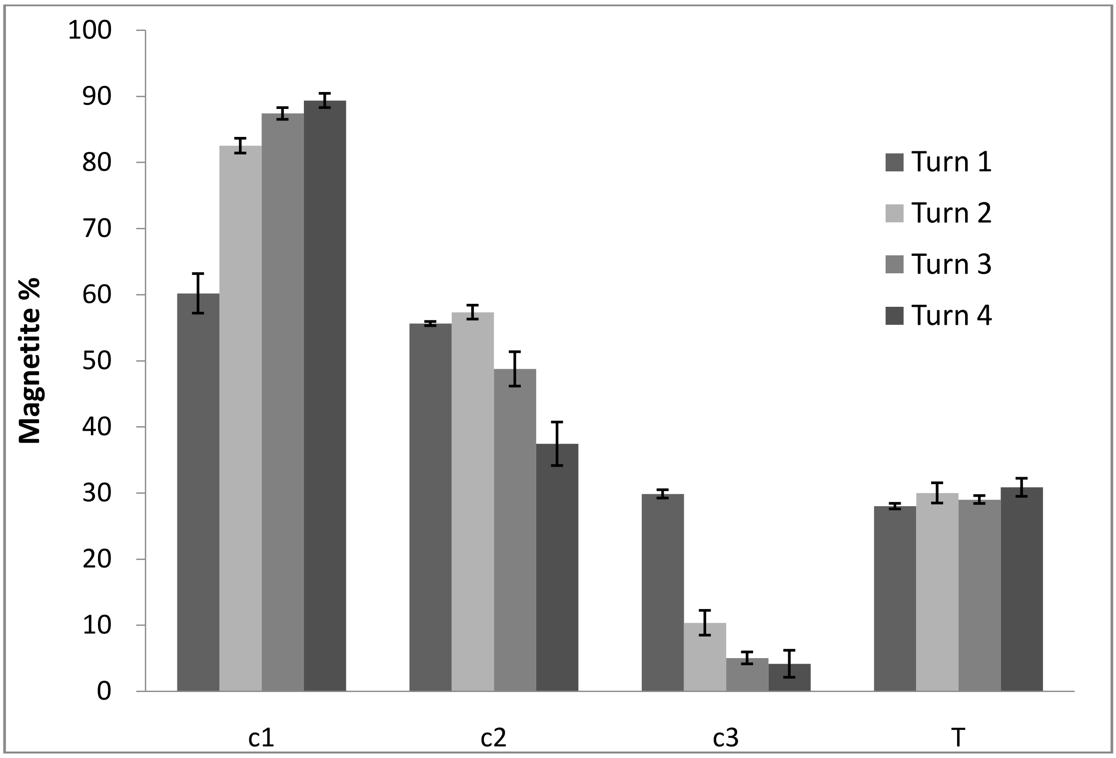

Figure 31 - The recovery of magnetite

Figure 32 shows the grade of magnetite in every channel as the turn number changes. The error bars represent the standard deviation of the measurements. The grade of magnetite in channel x is noted as $G_{m;x}$ and is calculated using:

$$G_{m;x} = \frac{W_{m;x}}{W_{S;x}} \qquad (4.2)$$

The variable $W_{m;x}$ represents the weight of magnetite reported to channel x, and $W_{S;x}$ represents the total weight of the solid reported to channel x.

As the number of turn increases, the increase in of the magnetite grade in C1 channel and the decrease in of the magnetite in C2 and C3 channels indicates a concentrating effect occurred between the middle zone and the inner zone of the spiral; this effect is most pronounced when the slurry travels from Turn 1 to Turn 2.

As shown in Figure 31 and Figure 32, while the recovery of magnetite decreases in the T channel, the grade of magnetite of the T channel remains unchanged, this observation indicates that the quartz in the tailing stream migrates inward simultaneously with magnetite from the T channel to the mid and inner zone. The size recovery curve for the quartz of T channel shown later confirms that the quartz in the spiral trough is also concentrated during the concentration process.

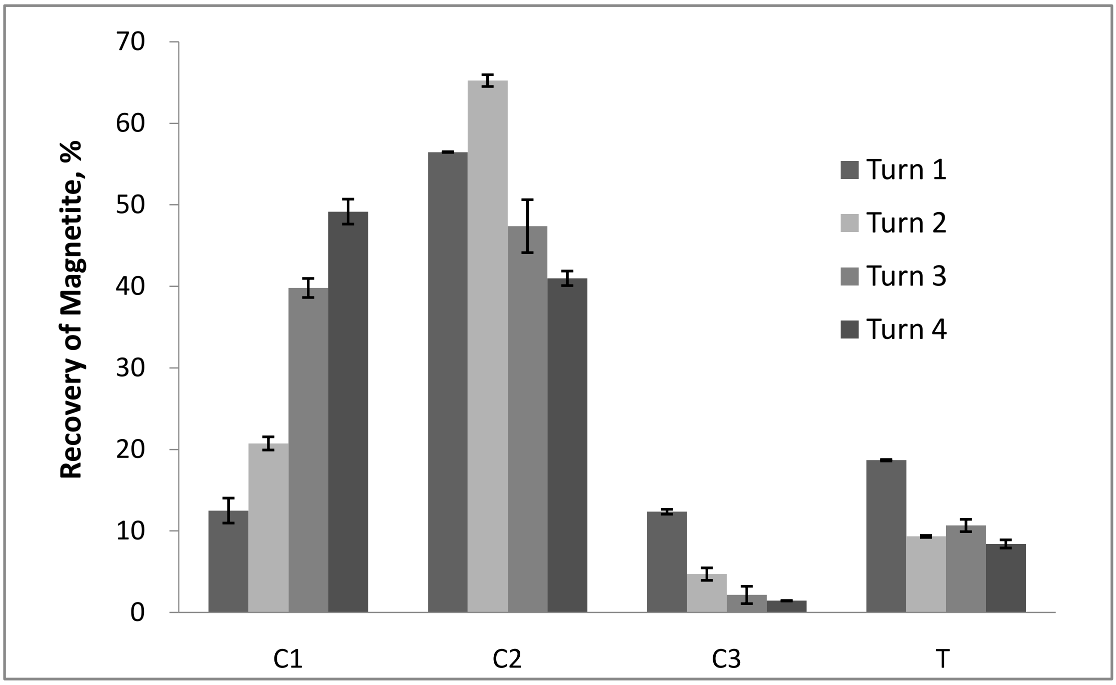

Figure 32 - The grade of magnetite of each channel in each turn of the spiral

Figure 33 shows the plot of cumulative recovery vs. the cumulative grade of magnetite in every turn. The error bars represent the standard deviation of the measurements. The first point on each curve represents the data collected from C1 channel on each turn, the second point on each curve represents the data collected from C2 channel plus the data of C1 channel, and so on, and the last point represents the data of all channels in this turn.

Thus, the values of grade at the last point on each curve are roughly same, which is the feed grade. The theoretical feed grade should be 41%, but the feed grades illustrated on the plots are all greater than 41%, this deviation might be caused by the inhomogeneous magnetite distribution in the feed tank. Since the exit of the feed tank is located at the bottom, and magnetite particles settle at a greater rate than quartz particles, as a result, the magnetite particles experience more frequent recirculation in this closed loop system. Therefore, the actual feed grade observed in the experiment is slightly higher than the theoretical feed grade calculated during the material preparation stage.

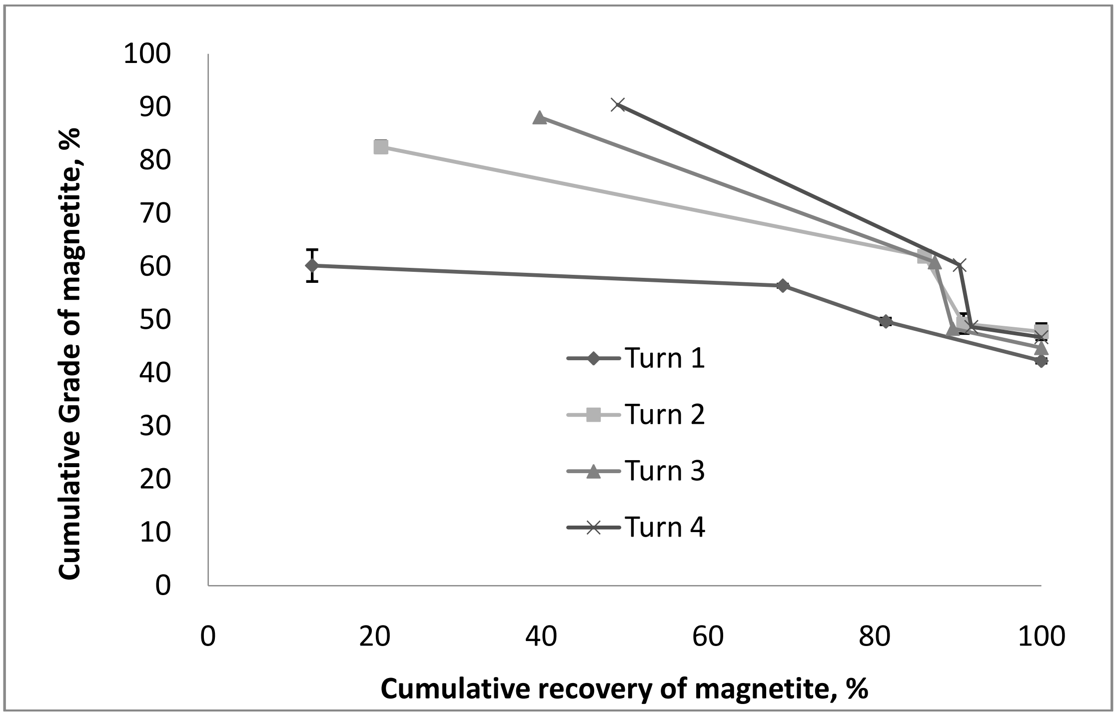

Figure 33 - Cumulative grade of magnetite vs. cumulative recovery of magnetite

4.7 Partition Curves of Magnetite and Quartz

The recovery or the partition factor for a channel x of a species i within size class d is noted as $R_{i;x;d}$ and is calculated using:

$$R_{i;x;d} = \frac{W_{i;x;d}}{W_{i;T;d}} \tag{4.3}$$

The variable $W_{i;x;d}$ represents the weight of species i within size class d collected from channel x, and $W_{i;T;d}$ represents the total weight of species i within size class d collected from all channels. The value of $W_{i;x;d}$ and $W_{i;T;d}$ are the values recorded during slurry analysis. The calculated recoveries ($R_{i;x;d}$) are plotted as a function of the mean size of the size class d to obtain the size recovery curves for species i in the channel x. The recovery curves for the magnetite in every channel are shown in Figure 34 to Figure 37.

The recovery of magnetite in C1 channel (see Figure 34) increases as the number of turns increases, this is more pronounced for the particles within the particle size range -300+106 µm. The recoveries of the magnetite from two extremes of the size fractions (-75 µm and +425 µm) has less change than the magnetite from the middle size fraction as the number of turn changes.

Similar results of low recovery of coarse particles have been reported by other researchers (Atasoy and Spottiswood, 1995; Bazin et al., 2014; Holland-Batt and Holtham, 1991; King et al., 1992; Richards et al., 2000). Some studies attributed the decrease in the recovery of coarse heavy particles to the Bagnold force that preferentially flushes coarse particles outward (Bouchard, 2001, Das et al., 2007). However, Figure 34 to Figure 37 show that the recoveries of coarse magnetite in all channels stay at a relative constant level, which demonstrates that the majority of the coarse magnetite always stays in the same stream from Turn 1 to Turn 4. This behaviour was also observed by Atasoy and Spottiswood (1995). Figure 35 shows that the majority of the coarse magnetite (+425 µm) stays in C2 channel. The recovery of magnetite particles within the size range -425+53 µm decreases while the number of turn increases. C3 channel seems to be an empty zone for all size fractions of magnetite particles, Batchelor (2000) revealed the same result. The recovery of magnetite and the level change of recovery are both low in this channel (see Figure 36). Figure 37 shows the partition curves of the magnetite for the tailing stream as the number of turn changes, the majority of the fine magnetite particles (-38 µm) are reported to this channel.

A remarkable observation is that 15% to 20% of the most coarse magnetite (-850+600 µm) particles stay in T channel from Turn 1 to Turn 4, indicating that the concentrating effect has only a very slight influence on these particles. A probable explanation could be the low pulp density in the tailing stream, which results a higher flow speed in the spiral trough that causes coarse magnetite particles be trapped inside the tailing stream instead of be concentrated to the inner streams.

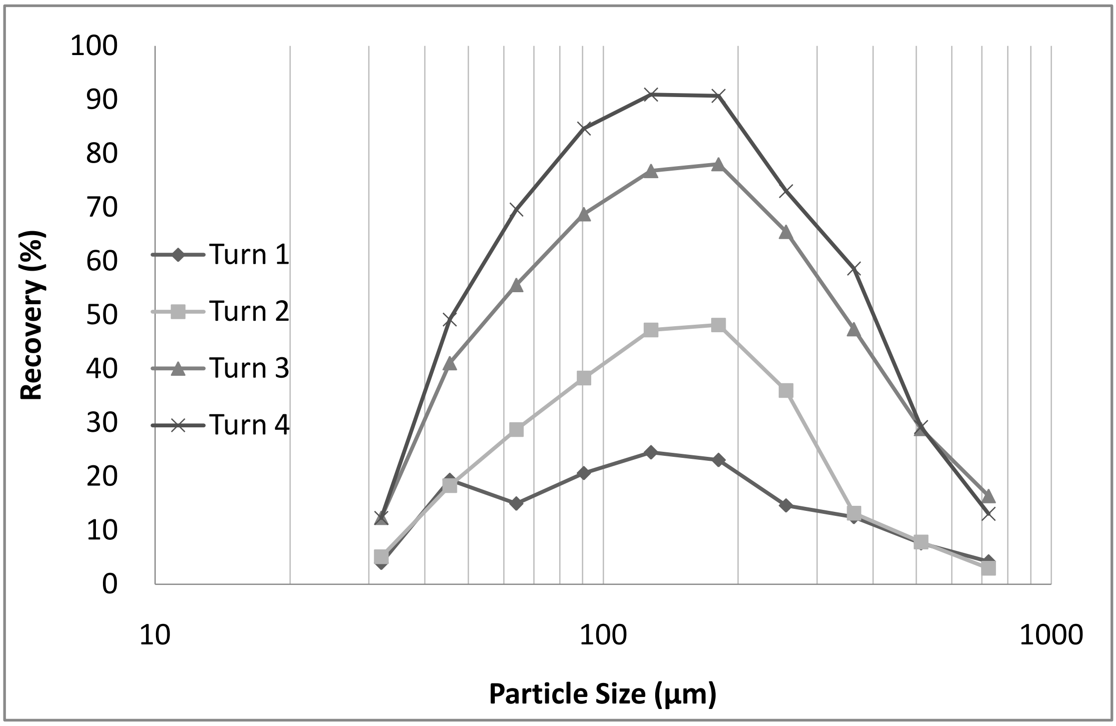

Figure 34 - Partition curves for magnetite of C1 channel

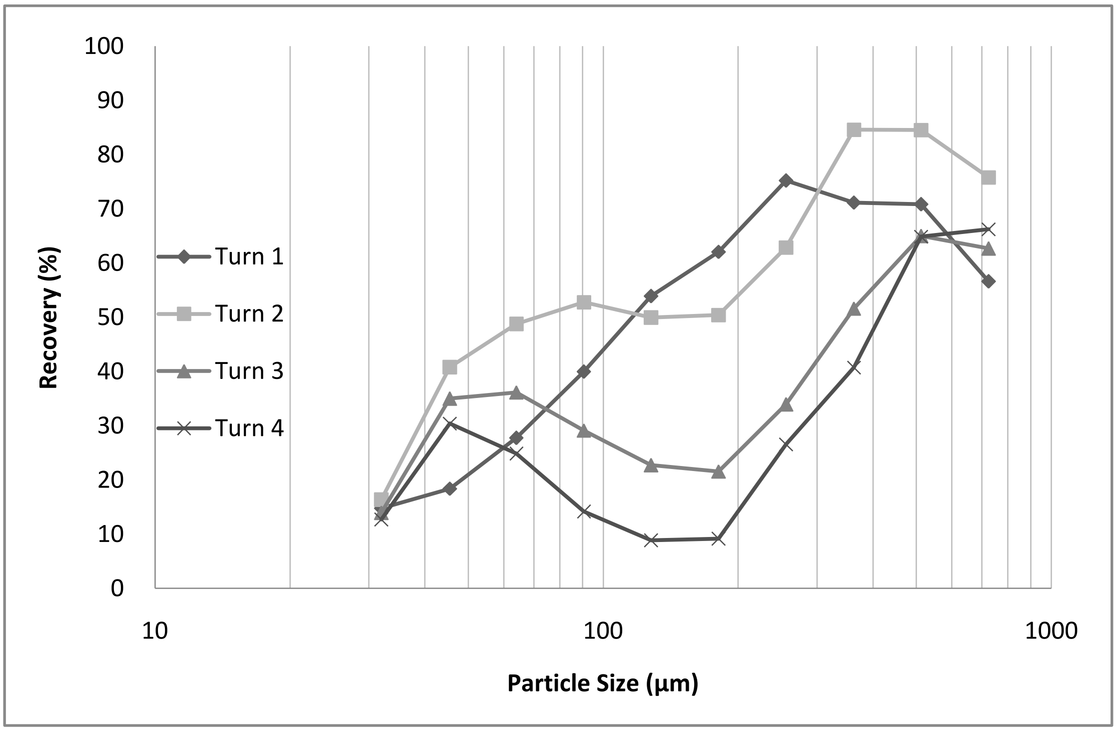

Figure 35 - Partition curves for magnetite of C2 channel

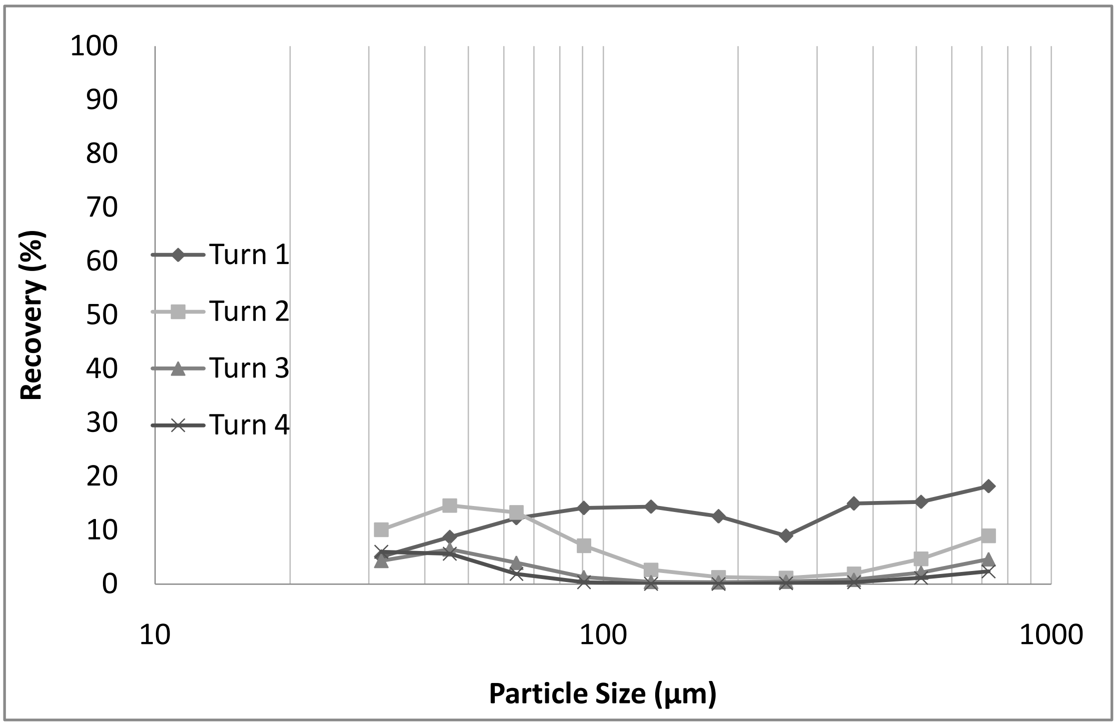

Figure 36 - Partition curves for magnetite of C3 channel

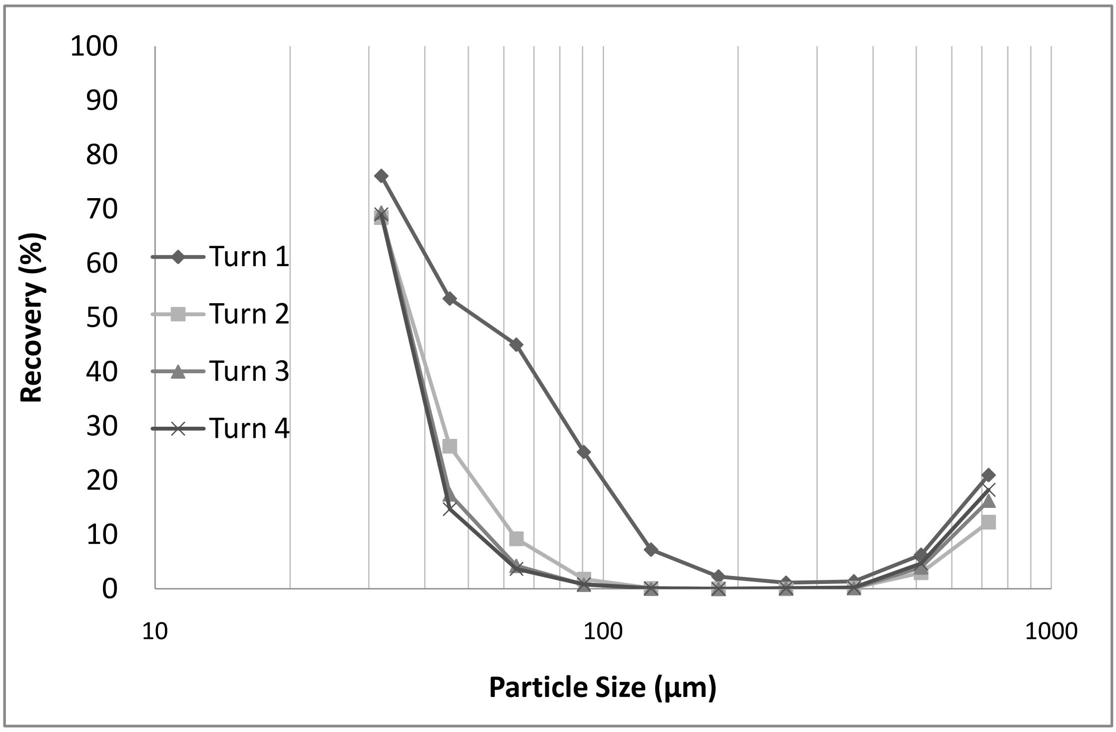

Figure 37 - Partition curves for magnetite of T channel

The partition curves of quartz for all channels are shown in Figure 38 to Figure 41. For C1 channel, the low recovery of quartz is anticipated; the quartz particles of middle size fraction exhibit the similar behaviors of the magnetite particles, the recovery of quartz from the size range (-300+106) has higher recovery than the particles from fine and coarse extremes. As shown in Figure 39, the majority of the middle size fraction quartz particles are reported to C2 at the end of process. In C3 channel, the recovery of quarts increases as the particle size increases. And in the T channel, the result is similar to the magnetite; fine and coarse particles are trapped in the tailing stream.

These observations demonstrate that the quartz particles have similar migration trend with the magnetite particles, the particles of middle size fraction are more active to the concentrating effect. However, due to the differences in specific gravity, the majority of the quartz particles migrates inward from the tailing stream, and accumulates in the middle streams (C2 and C3 channels). For the very fine and very coarse particles have less movement during the concentrating process, and preferentially stay in the stream from Turn 1 to the end.

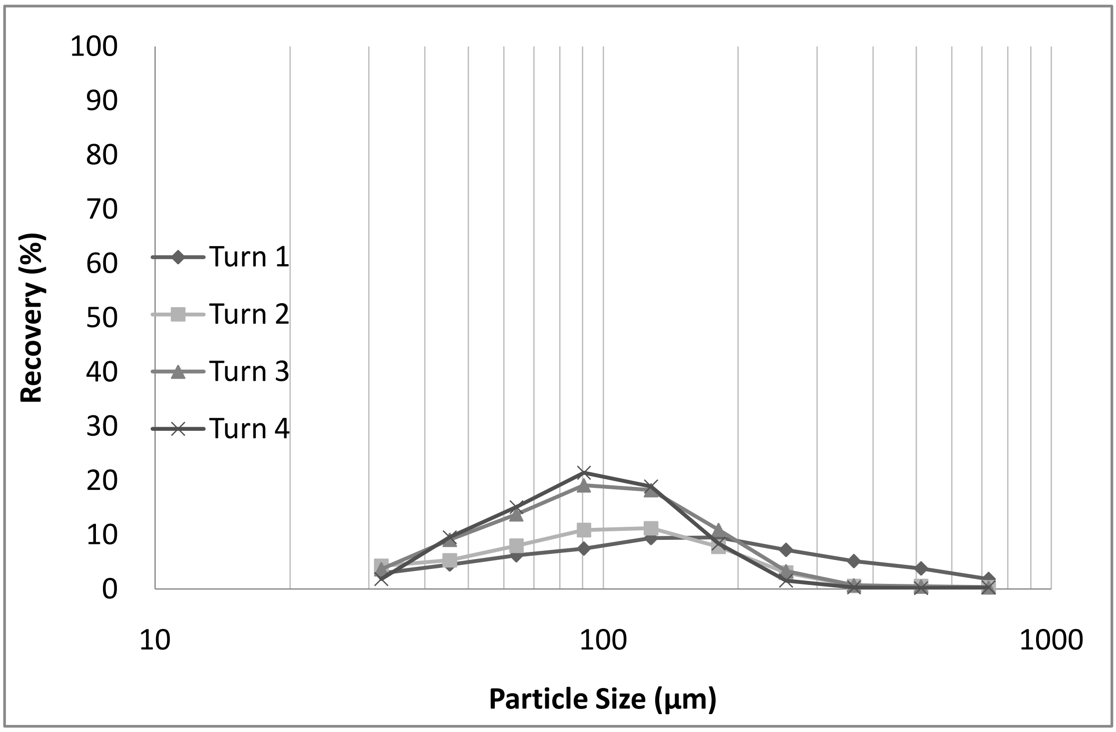

Figure 38 - Partition curves for quartz of C1 channel

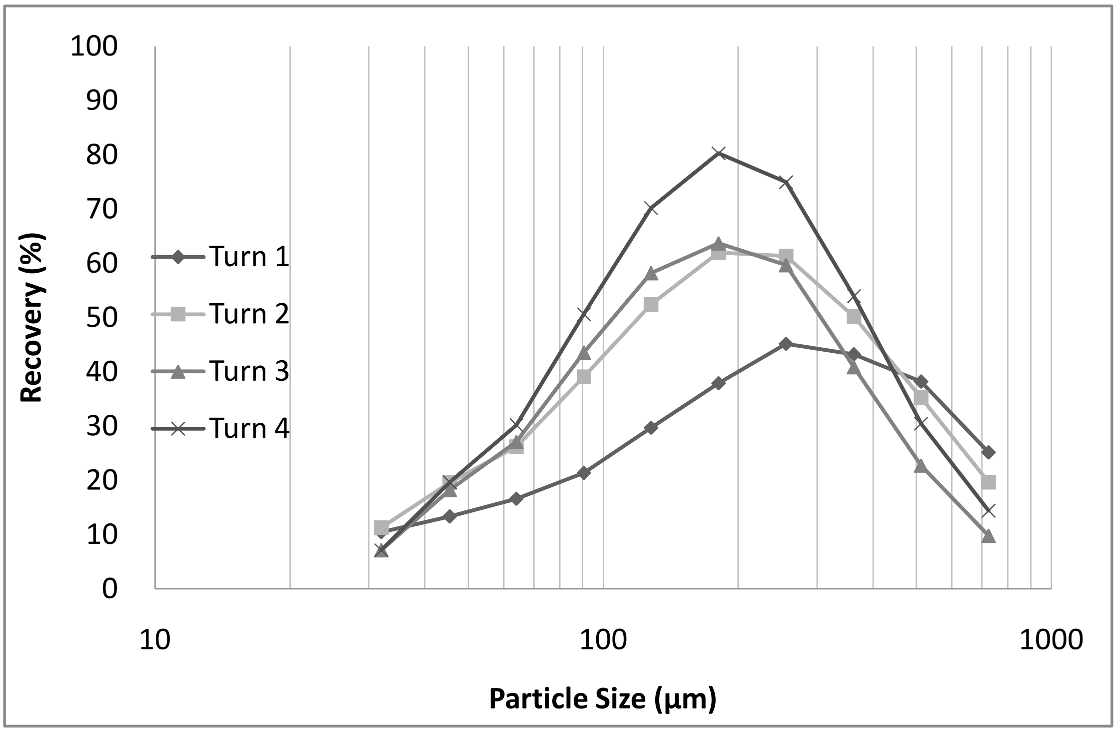

Figure 39 - Partition curves for quartz of C2 channel

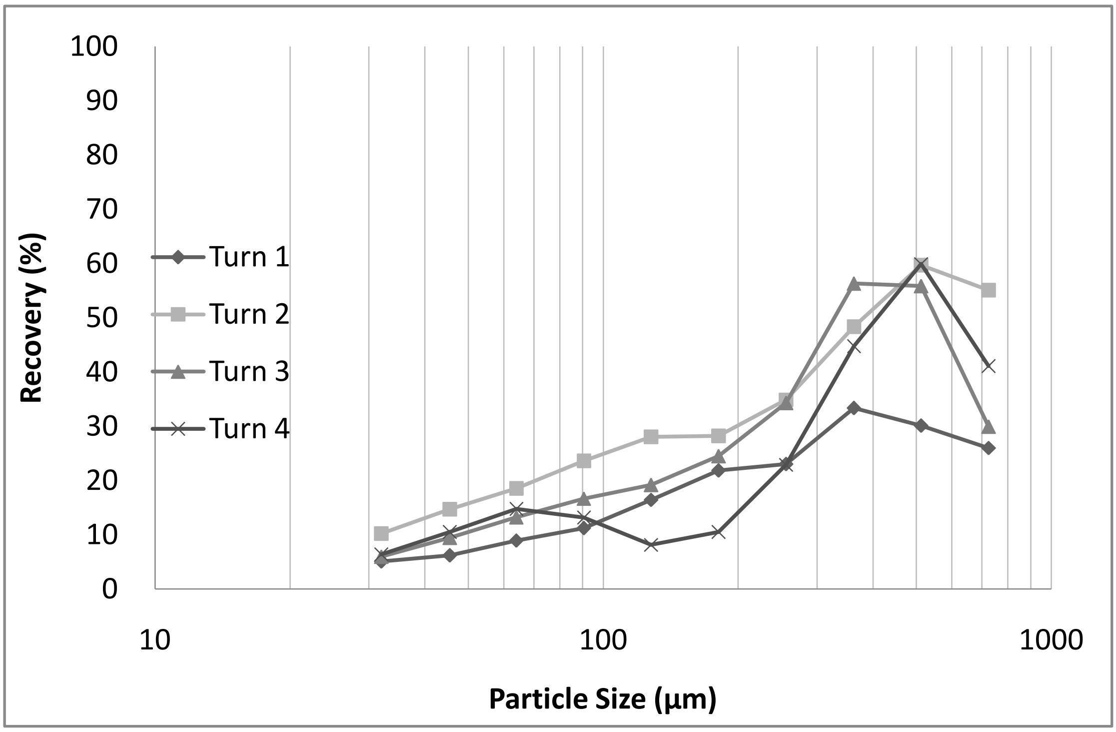

Figure 40 - Partition curves for quartz of C3 channel

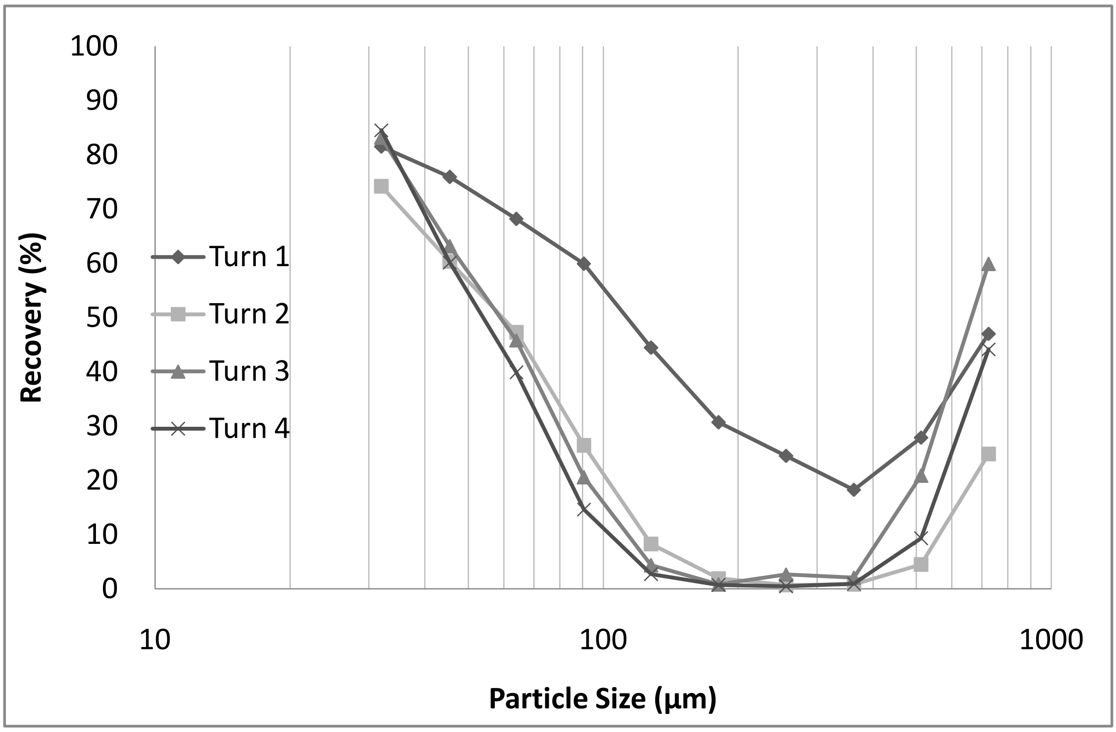

Figure 41 - Partition curves for quartz of T channel

4.8 Modeling of Partition Curves of Magnetite

The model developed by Bazin et al. (2014) is used in this section to model the partition curves of the magnetite on each turn of the spiral. According to Equation 2.57 and 2.58, the parameters that characterize the shape of a partition curve are Alpha S, Alpha P, d50 s, d50 p and Rp, these parameters are empirical. Rp is the total recovery of the magnetite which can be calculated from measured data; however, to determine the value of other parameters, the estimation is done by adjusting the value of parameter to make the modeled partition curves as close as possible to the observed partition curves. Table 14 shows the calibrated parameters that characterize the partition curves for each turn of the spiral concentrator. The modeled partition curves and the actual observed partition curves are shown in Figure 42.

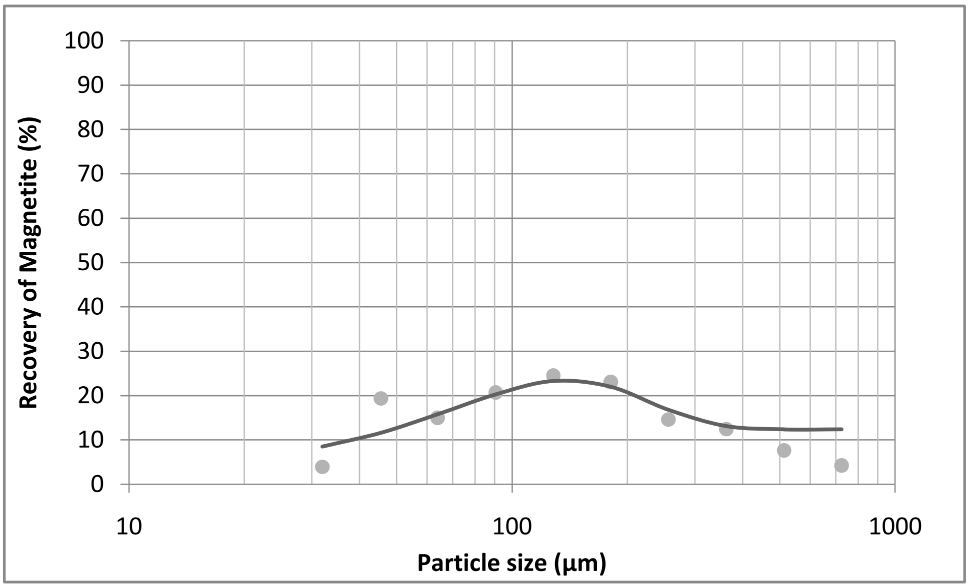

a) Turn 1

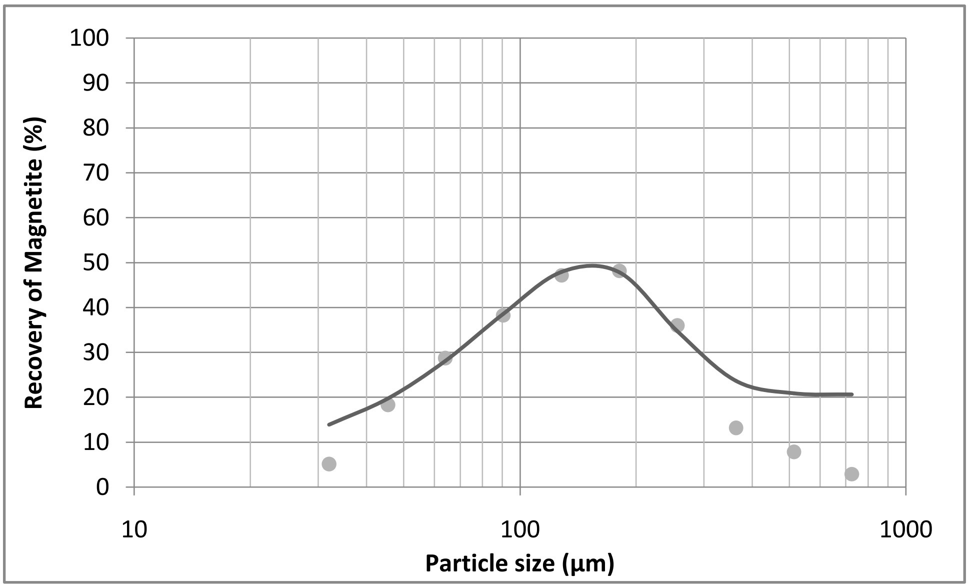

b) Turn 2

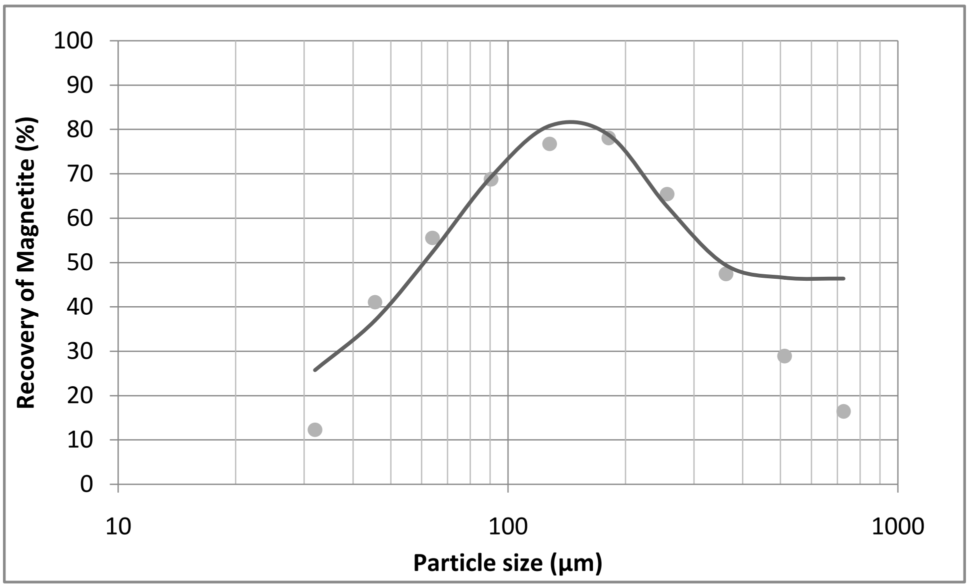

c) Turn 3

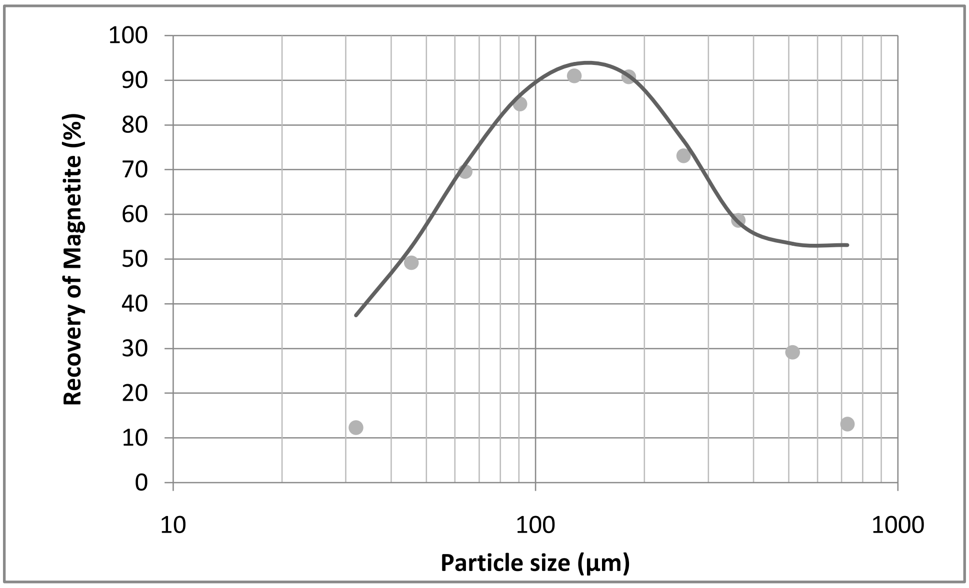

d) Turn 4

Figure 42 - Observed (symbols) and modeled (lines) partition curves for magnetite on each turn of the spiral concentrator

Table 14 - Parameters for the partition curve models

Turn	Alpha S	Alpha P	d50 s	d50 p	Rp
1	1.6	2	180	150	0.124
2	1.6	3	120	210	0.206
3	1.6	4	70	250	0.464
4	1.6	5	50	300	0.531

From Figure 42, it can be noticed that the modeled curves are well fitted with the observed partition curves in the middle particle size range (- 425+53 µm); for the fine size (-53 µm) and coarse size particles (+425 µm), the modeled data has a large deviation from the actual data. The explanation for this deviation can be found by observing the following graphs:

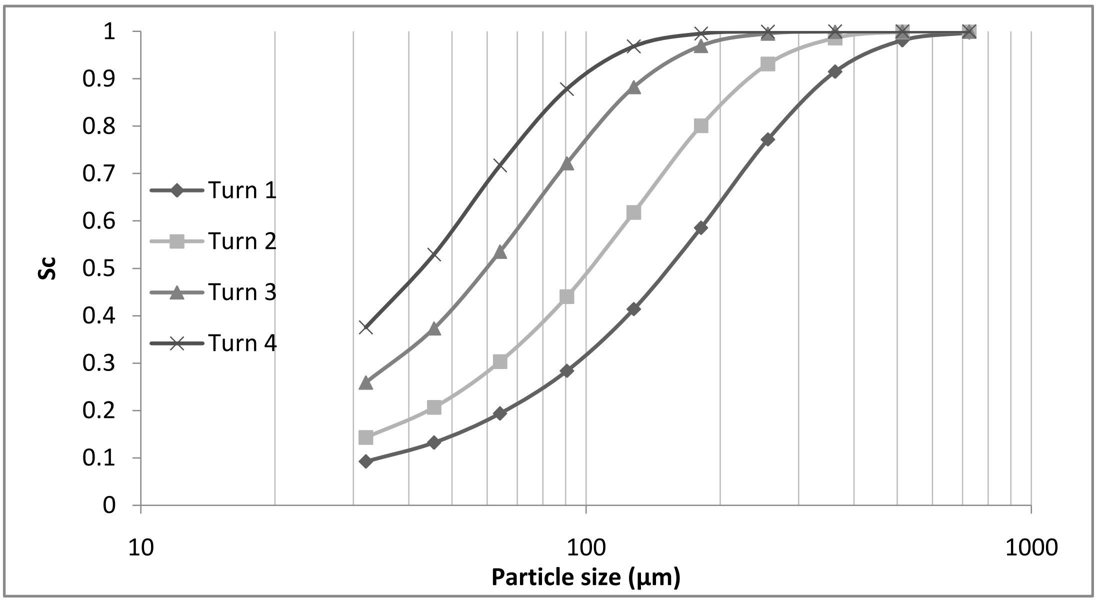

Figure 43 - S_C as a function of the particle size

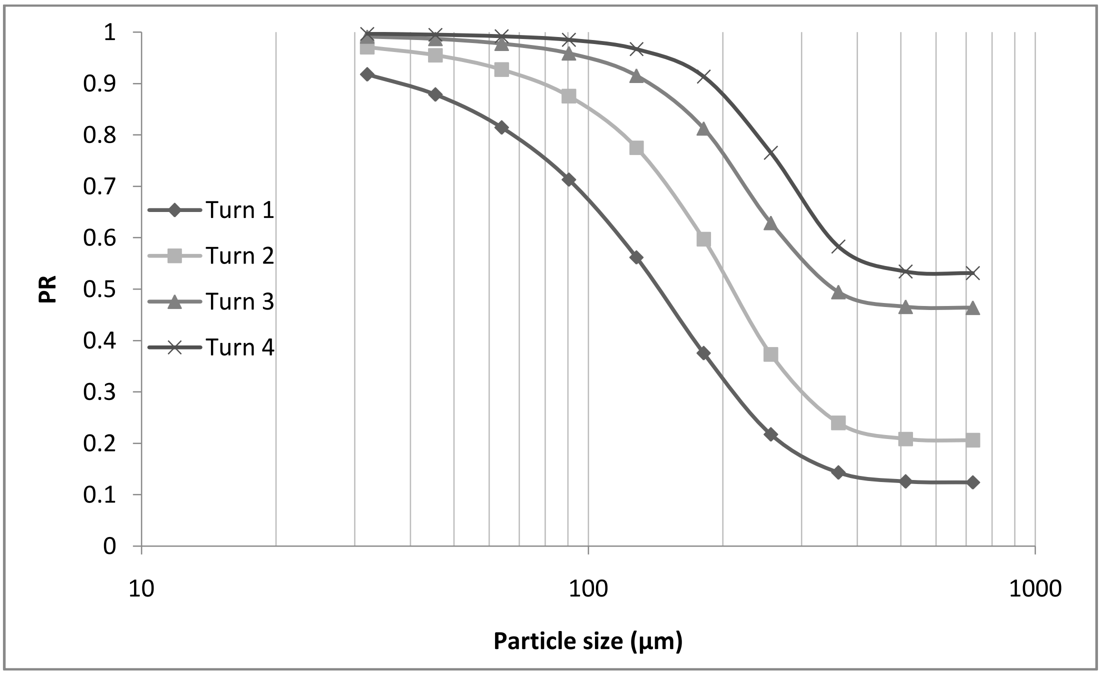

Figure 44 - P_R as a function of the particle size

Figure 43 and Figure 44 show the S_C and P_R as functions of the particle size for each turn of the spiral. According to Bazin et al. (2014), S_C represents the proportion of the feed that reports to the concentrate due to gravity force and P_R represents the proportion of the feed that resists to the outward force and reports to the concentrate. As shown in Figure 44, the model assumed the proportion of the feed that resists to the outward force decreases as the particles size increases until the particle size reaches approximately 400 µm; however, the observed data in this study indicates that the proportion of the particles that can resist to the outward force continuously decreases as the particle size increases until reaches the up limit of the particle size (850 µm). The model of Bazin et al. (2014) is developed for industrial spiral concentrators which are operating at a sweet spot, i.e. with optimal feed rate and pulp density. On the other hand, the spiral concentrator used in this study was operating with a feed rate higher than the recommended value and with a pulp density lower than the recommended value. Figure 45 shows the sweet spot for operating and the actual operating point of this study.

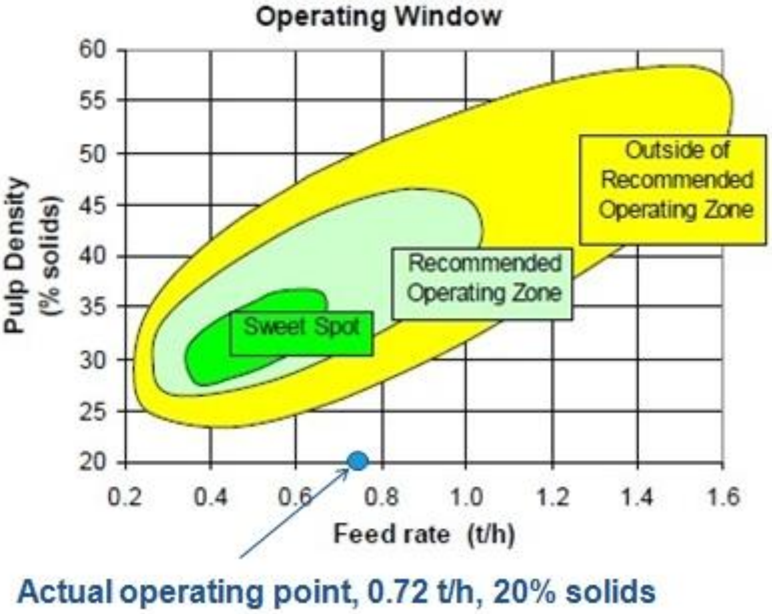

Actual operating point, 0.72 t/h, 20% solids

Figure 45 - The recommended operating parameter and the actual operating point

Due to the limitation of equipment used in the laboratory, the highest pulp density that the pump can sustain for a long term operation is 20%, any higher solid % feed would cause a blockage inside the pump; furthermore, to keep the pump continuously working with a slurry of 20% pulp density, the minimum flow rate is approximately 0.72 t/h, otherwise the feed rate would be hard to be maintained at a relatively constant level.

Despite the differences between the modeled and the observed partition curves at fine and coarse particle size, the model provides a satisfactory fit to the observed partition curve in middle particle size range. Figure 46 shows the parameters Alpha S, Alpha P as functions of the number of turns; and Figure 47 shows d50 s and d50 p as functions of the number of turns. According to the tendency to change revealed in Figure 46 and Figure 47, if one more turn were to be added to the spiral concentrator used in this study, the value of parameters for magnetite in Turn 5 can be predicted; and the partition curve for magnetite in Turn 5 is plotted in Figure 48

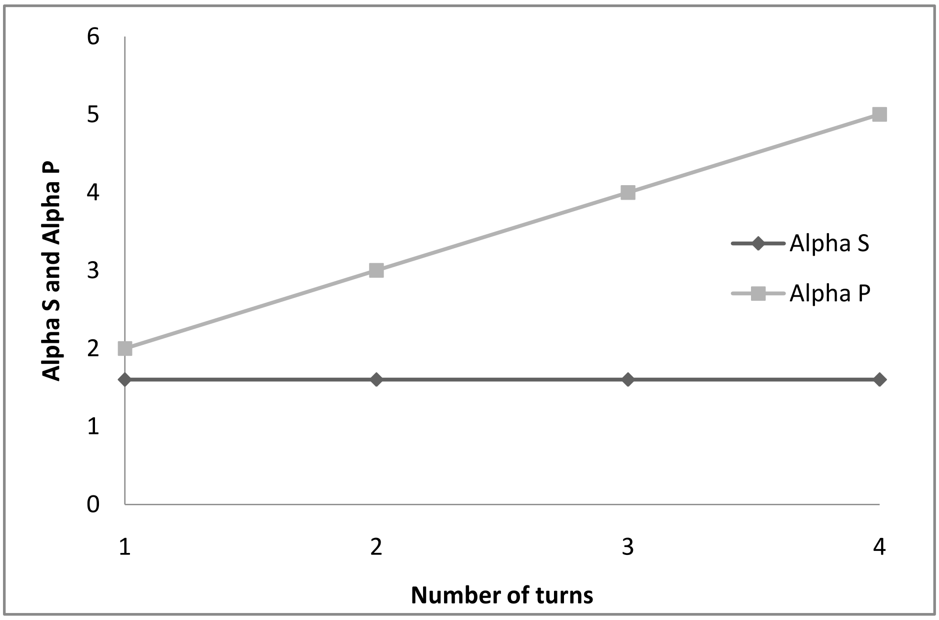

Figure 46 - Alpha S and Alpha P as function of number of turns

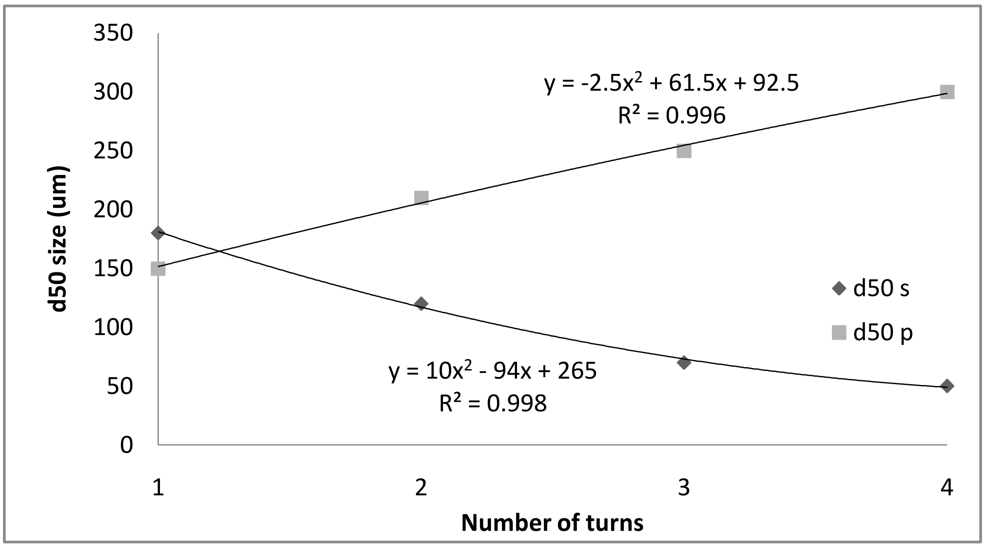

Figure 47 - d50 s and d50 p as function of number of turns

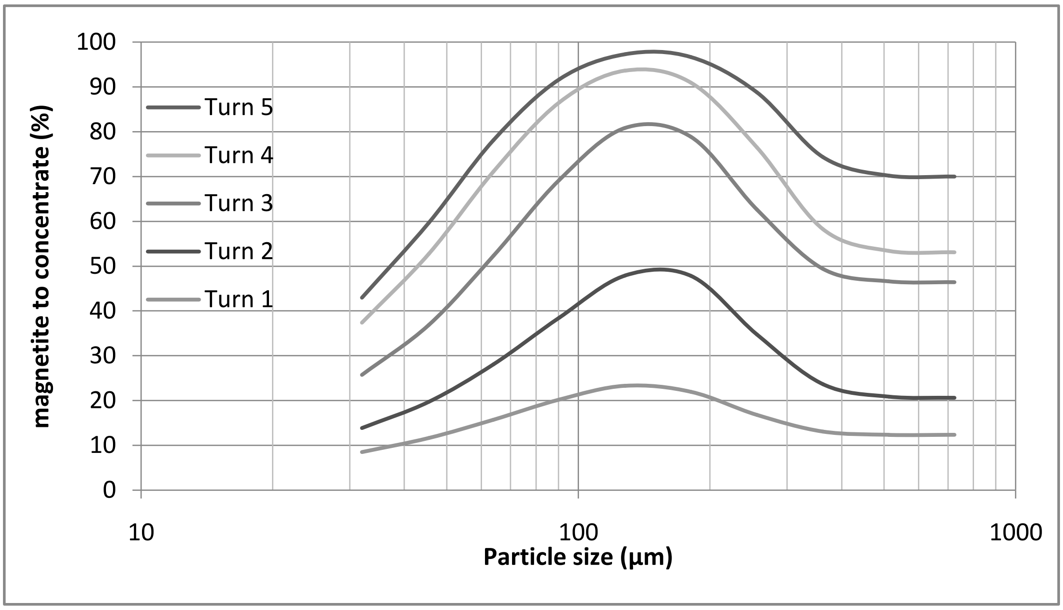

Figure 48 - The modeled partition curves

The modeled partition curve shown in Figure 48 indicates that the peak value of magnetite recovery can reach approximately 98% at Turn 5 which occurs when the particle size is around 150 µm. However, the overall recovery increment from Turn 4 to Turn 5 is much less than the increments achieved in the previous turns; in other words, the cost-performance ratio of adding Turn 5 on this spiral concentrator is low, the improvement of the middle size magnetite particles recovery is only just approximately 5%.

Chapter 5 - Conclusions and Recommendations

This study investigated the particle flow on a four turn spiral concentrator using a synthetic ore consisting of pure magnetite and quartz. The slurry samplings were conducted at the end of each turn to analyze the recoveries of both magnetite and quartz at different radial position across the trough of the spiral, which is divided into four independent channels to facilitate the investigation.

According the profile of the slurry, it can be concluded that, as the slurry travels along the spiral trough, the surface of the slurry becomes smoother and turbulence is reduced; moreover, the flow height becomes lower since the flow speed gets accelerated. The flow speed in the inner zone was approximately 8 cm/s, the middle zone was 20 cm - 30 cm/s and the flow speed for the outer stream is 110 cm to 200 cm/s.

The change in slurry viscosity is constantly taking place during the concentration process, the viscosity of the feed slurry is 1.23 mPa s. The viscosity of the tailing stream is always lower than feed slurry, and the viscosity of the flow in C1 channel increased most significantly, reaching 10 mPa s at Turn 3. However, the viscosity of the flow estimated in this study can be only applied to fully mixed slurry, it can provide an indication of solid migration trend; however, due to the settling of the heavy mineral particles, for different layers of the flow, their viscosities are also different.

The efficiency plots indicate an improvement of separation performance as the number of turns increases, the largest improvement occurred from Turn 1 to Turn 2. From Turn 3 to Turn 4, the efficiency improvement is least, this observation suggests that by adding more turns onto this model of spiral would get less and less separation efficiency; and this conclusion is proved by the modeling of the partition curve for the

Turn 5 on this spiral concentrator.

The partition curves show that the majority of magnetite particles of the middle size fraction (-300+106 µm) are concentrated to the C1 channel or the inner channel. The recovery of the magnetite particles from this size fraction has a significant increment as the number of turn increases. On other hand, the coarse magnetite particles (+600 µm) preferentially stay in the streams from Turn 1 to the last turn (Turn 4), especially for the coarse particles in the tailing stream which has a very high flow speed. The results also shown that the recovery of quartz to the inner channel is moderately low; the majority of the quartz particles of the middle particle size range report to channels C2 and C3. Similar to the magnetite, the very fine and very coarse quartz particles stay mostly in the tailing channel, the total movement inside the spiral trough during the process of these particles is much less than the particles of the middle particle size fraction.

The model developed by Bazin et al. (2014) was applied in this study to model the partition curves for each turn. Among ten particle size fractions, the modeled partition curves fit well with the observed partition curves for the seven fractions, which are located in the middle size range; alternatively, the modeled partition curves shown a large deviation with the observed partition curve at the very fine fraction and the very coarse fractions. A partition curve has been modeled for the virtual fifth turn of the spiral, the result shows that, by adding Turn 5 on this spiral concentrator the recovery improvement for middle size magnetite particles is low, barely 5%.

To conclude, the experimental set-up can satisfy the experimental conditions to achieve the objective of this study. To improve the quality of the study and reduce the standard deviation of the experimental results, higher precision slurry collectors are recommended, which can be made with metal and machined by CNC; for the slurry sampling method, the “bucket and stopwatch” method can be replace by a method with more precise timing. And lastly, in order to maximize the efficiency of the spiral concentrator, a pump that can work with higher pulp density slurry is recommended to use. The flow speed of a denser slurry will be slower, and as a result, the recovery of heavy mineral will be higher.

References

Allen, J.R.L., *Principles of Physical Sedimentology*. 1985, Allen & Unwin, London.

Atasoy, Y., Spottiswood, D.J., A study of particle separation in a spiral concentrator. Minerals Engineering, 1995, **8(10)**, 1197-1208.

Bagnold, R.A., Experiments on a gravity-free dispersion of large spheres in a newtonian fluid under shear. Proceedings of the Royal Society, London, 1954, **225**, 49-63.

Batchelor, G., *Introduction to Fluid Mechanics*. 2000, Cambridge University Press.
Bazin, C., Sadeghi, M., Roy, P., Bourassa, M., 2014. Simulation of an Iron Ore Concentration Circuit Using Mineral Size Recovery Curves of Industrial Spirals, In *46th Annual Canadian Mineral Processors Operators Conference*, Ottawa, Ontario, Canada.

Boucher, D., Deng, Z., Leadbeater, T., Langlois, R., Renaud, M., Waters, K.E., PEPT studies of heavy particle flow within a spiral concentrator. Minerals Engineering, 2014, **62**, 120-128.

Burt, R.O., *Gravity Concentration Technology*. 1984, Elsevier. , Amsterdam.

Das, S.K., Godiwalla, K.M., Panda, L., Bhattacharya, K.K., Singh, R., Mehrotra, S.P., Mathematical modeling of separation characteristics of a coal-washing spiral. International Journal of Mineral Processing, 2007, **84(1–4)**, 118-132.

Durand, R., The hydraulic transportation of coal and other materials in pipes. Proceedings of a Colloquium on the Hydraulic Transport of Coal, 1952, 39-52.

Falconer, A., Gravity Separation: Old Technique/New Methods. Physical Separation in Science and Engineering, 2003, **12(1)**, 31-48.

Fuerstenau, M.C., Han, K.N., *Principles of Mineral Processing*. 2003, Society for Mining, Metallurgy, and Exploration, Inc.

Gaudin, A.M., *Principles of Mineral Dressing*. 1939, McGraw-Hill Book Company, inc. - New York.

Glass, H.J., Minekus, N.J., Dalmijn, W.L., Mechanics of coal spirals. Minerals Engineering, 1999, **12(3)**, 271-280.

Gleeson, G.W., Why the Humphreys spiral works. Engineering and Mining Journal,

1945, **146**, 85-86.
Hanes, D.M., Inman, D.L., Observations of rapidly flowing granular-fluid materials. Journal of Fluid Mechanics, 1985, **150**, 357-380.

Holland-Batt, A.B., 1987. Spiral separation: theory and simulation, In *African Mining*, Zimbabew.

Holland-Batt, A.B., Interpretation of spiral and sluice tests. Transactions of The Institution of Mining and Metallurgy, 1990, **99**, C11-C20.

Holland-Batt, A.B., prediction of deposition velocities and their use in assessing sanding potential on spiral separators. The Institution of Mining and Metallurgy, 1992a**(101)**.

Holland-Batt, A.B., A study of the potential for improved separation of fine particles by use of rotating spirals. Minerals Engineering, 1992b, **5(10–12)**, 1099-1112.

Holland-Batt, A.B., The dynamics of sluice and spiral separations. Minerals Engineering, 1995, **8(1–2)**, 3-21.

Holland-Batt, A.B., Holtham, P.N., Particle and fluid motion on spiral separators. Minerals Engineering, 1991, **4(3–4)**, 457-482.

Holtham, P.N., Flow visualisation of secondary currents on spiral separators. Minerals Engineering, 1990, **3(3–4)**, 279-286.

Holtham, P.N., Particle transport in gravity concentrators and the Bagnold effect. Minerals Engineering, 1992a, **5(2)**, 205-221.

Holtham, P.N., Primary and secondary fluid velocities on spiral separators. Minerals Engineering, 1992b, **5(1)**, 79-91.

Hyma, D.B., Meech, J.A., Preliminary tests to improve the iron recovery from the -212 micron fraction of new spiral feed at quebec cartier mining company. Minerals Engineering, 1989, **2(4)**, 481-488.

Kapur, P.C., Meloy, T.P., Industrial modeling of spirals for optimal configuration and design: spiral geometry, fluid flow and forces on particles. Powder Technology, 1999, **102(3)**, 244-252.

Kelly, E.G., Subasinghe, G.K.N.S., Gravity performance curves: A re-examination. Minerals Engineering, 1991, **4(12)**, 1207-1218.

King, R.P., Juckes, A.H., Stirling, P.A., A Quantitative Model for the Prediction of the

Fine Coal Cleaning in a Spiral Concentrator. Coal preparation, 1992, **11(1-2)**, 51-66.
Loveday, B.K., Prediction of Gravity or Inertial Separation Efficiencies from Heavy Liquid Tests and Tromp Type Efficiency Curves: an Improved Method. Transactions of The Institution of Mining and Metallurgy, 1970, **Sect. C.**, C137-C140.

Loveday, G.K., 1993. The Modelling of Spiral concentrators, a thesis submitted in fulfilment of the requirements forr the degree of Master of Science in Department of Chemical Engineering. University of Cape Town.

Loveday, G.K., Cilliers, J.J., Fluid flow modelling on spiral concentrators. Minerals Engineering, 1994, **7(2–3)**, 223-237.

Miller, D.J., Design and operating experience with the Goldsworthy Mining Limited BATAC Jig and spiral separator iron ore beneficiation plant. Minerals Engineering, 1991, **4(3–4)**, 411-435.

Mine-Engineer.Com, 1994-2012. Splitter and discharge port of spiral. Information provided by Charles Kubach, Mining and Mineral Processing Engineer. Reference material, photos from Outokumpu

Mishra, B.K., Tripathy, A., A preliminary study of particle separation in spiral concentrators using DEM. International Journal of Mineral Processing, 2010, **94(3–4)**, 192-195.

Richards, R.G., MacHunter, D.M., Gates, P.J., Palmer, M.K., Gravity separation of ultra-fine (−0.1mm) minerals using spiral separators. Minerals Engineering, 2000, **13(1)**, 65-77.

Richards, R.G., Palmer, M.K., High capacity gravity separators: a review of current status. Minerals Engineering, 1997, **10(9)**, 975-982.

Richardson, J.F., Zaki, W.N., The sedimentation of a suspension of uniform spheres under conditions of viscous flow. Chemical Engineering Science, 1954, **3(2)**, 65-73.

Richardson, J.F., Zaki, W.N., Sedimentation and fluidisation: Part I. Chemical Engineering Research and Design, 1997, **75,** S82-S100.

Sadeghi, M., Bazin, C., Renaud, M., Effect of wash water on the mineral size recovery curves in a spiral concentrator used for iron ore processing. International Journal of Mineral Processing, 2014, **129**, 22-26.

Sikdar, S.K., Ore, F., Viscosity Measurements of Non-Newtonian Slurry Suspensions Using Rotating Viscometers. Industrial & Engineering Chemistry Process Design and Development 1979, **18(4)**, 722-728.

Sivamohan, R., Forssberg, E., Principles of spiral concentration. International Journal of Mineral Processing, 1985, **15(3)**, 173-181.

Thomas, D.G., Transport characteristics of suspension: VIII. A note on the viscosity of Newtonian suspensions of uniform spherical particles. J. Colloid Sci., 1965, **20(3)**, 267.

Tromp, K.F., *New Method of Computing the Washability of Coals*. 1937, Colliery Guard.

Tucker, P., An approach to modelling industrial unit processes: application to a spiral concentrator for minerals. Applied Mathematical Modelling, 1985, **9(5)**, 375-379.

Yalin, M.S., *Mechanics of Sediment Transport*. 1977, Pergamon Press.

Appendix

Table 15 - Magnetite recovered in Turn 1 for each channel (g)

Particle Size (μm)	C1	C2	C3	T
850	1.06	14.30	4.60	5.30
600	3.48	32.45	7.01	2.87
425	4.52	25.79	5.43	0.50
300	7.02	36.05	4.30	0.56
212	5.33	14.34	2.91	0.52
150	4.07	8.95	2.39	1.20
106	2.27	4.40	1.56	2.78
75	1.19	2.20	0.97	3.56
53	1.63	1.54	0.73	4.48
38	1.39	5.16	1.78	26.54

Table 16 - Magnetite recovered in Turn 2 for each channel (g)

Particle Size (μm)	C1	C2	C3	T
850	1.51	39.07	4.61	6.32
600	6.14	66.49	3.67	2.31
425	9.01	57.85	1.34	0.15
300	23.61	41.31	0.71	0.03
212	17.65	18.47	0.48	0.01
150	11.59	12.26	0.66	0.04
106	5.81	8.02	1.08	0.27
75	2.66	4.51	1.23	0.85
53	1.42	3.16	1.13	2.03
38	1.84	5.88	3.64	24.62

Table 17 - Magnetite recovered in Turn 3 for each channel (g)

Particle Size (μm)	C1	C2	C3	T
850	7.56	28.89	2.13	7.50
600	19.43	43.74	1.44	2.68
425	29.80	32.44	0.51	0.10
300	38.34	19.87	0.26	0.08
212	29.33	8.11	0.12	0.01
150	19.94	5.90	0.11	0.01
106	11.47	4.86	0.22	0.13
75	5.51	3.58	0.39	0.42
53	3.16	2.69	0.50	1.34
38	3.66	4.14	1.28	20.60

Table 18 - Magnetite recovered in Turn 4 for each channel (g)

Particle Size (μm)	C1	C2	C3	T
850	4.42	22.41	0.81	6.18
600	16.52	36.72	0.67	2.65
425	31.21	21.70	0.17	0.15
300	37.82	13.77	0.10	0.07
212	28.92	2.92	0.02	0.01
150	20.51	2.00	0.01	0.03
106	12.23	2.05	0.05	0.12
75	5.96	2.13	0.16	0.31
53	3.54	2.19	0.40	1.06
38	3.73	3.86	1.81	20.96

Table 19 - Quartz recovered in Turn 1 for each channel (g)

Particle Size (μm)	C1	C2	C3	T
850	0.48	6.56	6.79	12.27
600	1.65	16.60	13.09	12.13
425	2.61	21.90	16.91	9.26
300	5.00	31.31	15.97	16.99
212	4.58	18.29	10.53	14.81
150	2.80	8.88	4.91	13.27
106	1.67	4.78	2.51	13.38
75	0.79	2.10	1.13	8.62
53	0.37	1.08	0.50	6.12
38	1.19	4.33	2.10	33.65

Table 20 - Quartz recovered in Turn 2 for each channel (g)

Particle Size (μm)	C1	C2	C3	T
850	0.12	6.28	17.59	7.93
600	0.31	20.72	35.09	2.65
425	0.52	41.32	39.82	0.69
300	2.65	53.65	30.56	0.62
212	4.19	33.33	15.16	1.06
150	3.69	17.18	9.20	2.71
106	2.51	9.03	5.45	6.11
75	1.03	3.37	2.38	6.07
53	0.45	1.66	1.25	5.12
38	1.72	4.57	4.14	30.04

Table 21- Quartz recovered in Turn 3 for each channel (g)

Particle Size (µm)	C1	C2	C3	T
850	0.12	3.41	10.43	20.86
600	0.23	11.12	27.30	10.22
425	0.47	26.92	37.09	1.37
300	2.60	46.82	26.90	2.12
212	6.24	36.25	13.95	0.48
150	6.08	19.40	6.39	1.47
106	4.57	10.39	3.98	4.91
75	1.69	3.32	1.62	5.61
53	0.74	1.49	0.77	5.16
38	1.50	2.94	2.46	34.23

Table 22 - Quartz recovered in Turn 4 for each channel (g)

Particle Size (µm)	C1	C2	C3	T
850	0.09	4.02	11.45	12.32
600	0.10	13.69	26.91	4.19
425	0.17	31.20	25.89	0.56
300	1.14	55.02	16.83	0.36
212	4.00	38.10	4.99	0.34
150	5.69	21.15	2.47	0.82
106	4.93	11.67	3.04	3.38
75	1.82	3.63	1.77	4.80
53	0.80	1.63	0.87	4.99
38	0.85	3.31	2.94	38.93